Draft version April 15, 2024
Typeset using LaTeX **twocolumn** style in AASTeX631

Flashlights: Microlensing vs Stellar Variability of Transients in the Star Clusters of the Dragon Arc

Sung Kei Li [1], Patrick L. Kelly [2], Jose M. Diego [3], Jeremy Lim [1], WenLei Chen [4], Amruth Alfred [1], Liliya L.R. Williams [2], Thomas J. Broadhurst [5,6,7], Ashish K. Meena [8], Adi Zitrin [8] and Alex Chow [1]

[1] *Department of Physics, The University of Hong Kong, Pokfulam Road, Hong Kong*
[2] *Minnesota Institute for Astrophysics, University of Minnesota, 116 Church St. SE, Minneapolis, MN 55455*
[3] *IFCA, Instituto de Física de Cantabria (UC-CSIC), Av. de Los Castros s/n, 39005 Santander, Spain*
[4] *Department of Physics, Oklahoma State University, 145 Physical Sciences Bldg, Stillwater, OK 74078, USA*
[5] *Department of Theoretical Physics, University of Basque Country UPV/EHU, Bilbao, Spain*
[6] *IKERBASQUE, Basque Foundation for Science, Bilbao, Spain*
[7] *Donostia International Physics Center, Paseo Manuel de Lardizabal, 4, San Sebastián, 20018, Spain*
[8] *Department of Physics, Ben-Gurion University of the Negev, PO Box 653, Be'er-Sheva 8410501, Israel*

ABSTRACT

We study the nature of transient events detected in the "Dragon Arc", a star-forming galaxy at a redshift of 0.7251 that is gravitationally lensed by the galaxy cluster Abell 370. In particular, we focus on a subset of ten transients that are identified as unresolved young star clusters in the deep broadband, F200LP, taken as part of the "Flashlights" Hubble Space Telescope program, showing flux variations of $\sim 10-20\%$ over a period of about a year. Here we develop several methods to address whether stellar microlensing alone is capable of explaining the transients, or whether intrinsic stellar outbursts or variability are required to explain them. We first present a lens model that has new constraints in the Dragon Arc itself to understand the properties of the lensed young star clusters. Using our improved galaxy-cluster lens model, we simulate the effect of microlensing on the flux variation for unresolved stars within lensed young star clusters. We find good agreement between the observed and the expected detection rates of microlensing events by intracluster stars of young star clusters within 1σ. However, we cannot fully exclude the possibility that a minority of these transients are caused by intrinsic stellar variability such as outbursts of Luminous Blue Variables (LBVs). With JWST observations taken recently or coming in the near future, the color information will be able to break the degeneracy and definitively test whether or not these lensed young star cluster transients are caused by stellar microlensing.

Keywords: Galaxy clusters (584), Gravitational microlensing (672), Strong gravitational lensing (1643), Young star clusters (1833)

1. INTRODUCTION

With virial masses of order 10^{15} $M_\odot$, galaxy clusters are the most powerful gravitational lenses, generating hundreds of multiply lensed images of background galaxies in deep Hubble and JWST data. Some of these lensed galaxies are crossed by the critical curve, so that the magnification varies within a lensed arc and can be extreme near the critical curve. The maximum magnification of an object that is intersecting the caustic is inversely proportional to its size, R, or more precisely to the square root of its size, that is $\mu_{max} \propto 1/\sqrt{R}$ so that for stars in the process of crossing a caustic this can reach factors of 10^6, in principle (Miralda-Escude 1991). In practice, the ubiquitous presence of microlenses (for instance intracluster stars) or millilenses (for instance globular clusters in the intracluster medium, or ICM) lowers the maximum magnification at the cluster caustic resulting in maximum magnification factors $\sim 10^5$ or less (Venumadhav et al. 2017; Diego et al. 2018). Despite this reduction in the maximum magnification, it is still enough to observe individual stars in the background galaxy which would be otherwise ~ 10 magnitudes fainter and remain undetected. Near cluster caus-

keihk98@connect.hku.hk

tics, microlenses are most likely to intersect the line of sight to background stars, and produce fluctuations in the observed flux that can be used to recognize these distant stars. The first such event was Icarus (Kelly et al. 2018), but it was quickly followed by many other examples.

Icarus was discovered as part of an SN discovery campaign in the field of the galaxy cluster MACS J1149.5+2223 ($z = 0.54$). Images of this cluster were taken with the Hubble Space Telescope (HST) at different epochs. By making differences of images taken with the same filter, a sudden increase in brightness was found at the position of a point source lying very close to the critical curve. This source belongs to a lensed spiral galaxy at $z = 1.49$, and remained unresolved despite the large magnification factor implied by several lens models. Given its unresolved nature, the source was constrained to be comparable in size to a luminous star ($\lesssim 0.06$ pc). Its Spectral Energy Distribution (SED) is well described by a blue supergiant star, thus ruling out the supernova explosion scenario as the reason for the change in brightness. This star was dubbed "Icarus" Kelly et al. (2018) and represents the first of a rapidly growing list of individual stars detected at cosmological distances. Because of the duration of the transient event in Icarus, the change in flux was interpreted as due to a microlens that momentarily aligned with the distant star. More microlensing events are expected in the future as different microlenses move in front of Icarus. Not long after the discovery of "Icarus", several more microlensing event candidates were recognized, including "Spock" (Rodney et al. 2018) and "Warhol" (Chen et al. 2019), and the "FLashlights" program has been initiated for a systematic dedicated study of this lensed transient phenomenon behind a set of the best known lensing clusters(Kelly et al. 2023) which continuously yields new examples, including those analyzed here that are associated with the Dragon Arc.

During a microlensing event, the flux of a lensed star can change ~ 2 magnitudes but since the peak of these events is relatively short-lived (a few weeks at most), repeated observations of the same region may capture the flux change due to microlensing away from the peak emission, and hence with a relatively small change in flux of less than one magnitude. Specially designed observations can maximize the chance of observing microlensing events. Since intrinsically fainter stars are more abundant, deeper observations are a natural way of increasing the number of microlensing events. In addition, two observations made with the same position angle of the telescope result in better-subtracted images, since asymmetries in the PSF (for instance diffraction spikes) cancel out exactly leaving only photon noise around bright sources and instrumental noise as the main sources of uncertainty. Transients can then be identified more easily in such a way.

This strategy was recently followed by the Flashlights program (Kelly et al. 2022). This program targets the six galaxy clusters observed in the Hubble Frontier Field (HFF) program (Lotz et al. 2017) in two visits separated approximately one year apart. In each epoch, images are acquired with the widest filters available in WFC3, UVIS F200LP and F350LP, and at the same position angle in all observations of each cluster. In this way, changes in brightness caused by PSF differences due to the rotation of the telescope's mirror can be avoided. PSF differences can otherwise be mistaken for transients.

More recently, inspired by the success of HST and the Flashlights program, JWST data is being used to search for additional microlensing events. While HST is more sensitive to blue supergiants, JWST data is better suited for red supergiants since these stars are brighter in the infrared. Several distant stars have been found with JWST (e.g., Diego et al. 2023; Meena et al. 2023a)

Studying these caustic crossing events provides valuable insight into the distant lensed stars, but also about the intervening microlenses. By studying the event rate, one can look into the abundance of luminous stellar populations in galaxies in the early universe (e.g.: Schauer et al. 2022; Diego et al. 2023). Not limited to studying these lensed stars themselves, one can also use these events to probe the properties of stars in the ICM or even the nature of Dark Matter (DM). For example, in Kelly et al. (2018), light curves are simulated assuming different assumptions about the stars in the ICM, and a possible population of primordial black holes (a DM candidate). They found that, for a single cluster model, the Salpeter mass function (Salpeter 1955), where the abundance of low-mass stars follows a power law distribution, is preferred over the Chabrier mass function (Chabrier 2003), where the abundance of low-mass stars follows a log-normal distribution, as the mass function of stars in the ICM; Diego et al. (2018) and Oguri et al. (2018) placed an upper limit on the fraction of Primordial Black Holes (PBHs) with mass of order of $\sim 1 - 100 M_\odot$ in DM with Icarus. The former work found that if PBHs take up more than 3% of DM, there would be significantly more peaks in the light curve of Icarus; The latter work claimed that if PBHs take up more than 10% of DM, they would saturate the lensing magnification at the position of Icarus where it would

have never had sufficient magnification to be detectable.

Here, we focus on the Flashlights, and images of the galaxy cluster Abell 370 (A370) at $z = 0.375$ (Struble & Rood 1999). We supplement this data with additional observations from the HFF program. The two visits from Flashlights are separated by 331 days (at MJD 58907 and 59236), about five years later than the majority of images taken in the HFF observations of this cluster (MJD $\approx$ 57400). Multiple transients have been detected based on a comparison of the two Flashlights images alone (Kelly et al. 2022; Meena et al. 2023b), where almost all of them reside in the largest lensed arc visible in the A370 field, dubbed the "Dragon Arc". This arc is famously known for being the first recognized gravitationally-lensed giant arc (Soucail et al. 1987a,b,c), and has since been shown to correspond to a late-type galaxy at a redshift of $z = 0.7251$ (Soucail et al. 1988; Treu et al. 2015; Lagattuta et al. 2017; Diego et al. 2018).

As expected, many of the transients found in this arc are close to critical curves predicted by multiple lens models, where the magnification is greatest. Also, there is no signal detected in their position during the HFF epochs and hence, they are likely to be candidates for caustic crossing events. Some other transients appear at the position of unresolved knots in the Dragon Arc that are farther away from critical curves. These knots are found to be young star clusters based on their Spectral Energy Distribution (SED) fitting, with inferred stellar masses of the order of $\sim 10^4 M_\odot$ and very young age of $\sim 1 - 10$ Myr. For those more magnified and thus brighter ones, we are also capable of retrieving their spectra from Multi-Unit Spectroscopic Explorer (MUSE) (Bacon et al. 2010) and finding multiple emission lines (e.g., [OIII] and H-β, see Appendix), further affirming their young star cluster nature. We classify young star clusters that show $\geq 3\sigma$ change in brightness as transients and found nine extra transients, apart from the one that is already reported in Kelly et al. (2022). All these ten lensed young star cluster transients are shown by colored circles in Figure 1, and are listed in Table 1.

As these knots are young star clusters, and hence much bigger than individual stars, caustic crossing events that feature a single star being microlensed are not necessarily the best explanation for their brightness variation, since that relative change in flux due to microlensing is likely too small to be noticeable. Here in this paper, we explore in detail if these lensed young star cluster transients are caused by intrinsic stellar outbursts within, or if they can still be explained by stellar microlensing acting on the whole young star cluster.

Table 1. Compact knot Transients

Knot Transient	$\Delta\alpha('')$	$\Delta\delta('')$	Δm	$\lvert\mu\rvert$
1	10.88	-6.67	0.19 ± 0.04	7.90
2	9.68	-6.30	0.13 ± 0.04	9.51
3	7.67	-7.78	0.07 ± 0.02	14.45
4	0.23	-10.51	-0.26 ± 0.04	27.97
5	-0.16	-9.27	0.18 ± 0.05	40.01
6*	-0.84	-9.38	0.16 ± 0.02	13.70
7	-1.93	-9.67	0.14 ± 0.04	18.63
8*	-10.43	-6.86	0.09 ± 0.02	10.40
9	-10.82	-6.73	0.44 ± 0.08	9.77
10	-11.00	-6.92	0.19 ± 0.06	9.75

[a] $\Delta\alpha('')$ and $\Delta\delta('')$ are relative to the reference coordinate ($\alpha = 39.97134$, $\delta = -1.5822597$).

[b] Transients denoted with asterisk are multiply-lensed

To test whether intrinsic stellar outbursts can explain some of the transients, we made use of one of the transients as a case study. This transient is knot 2.6.2 as highlighted with a green arrow in the middle of both panels in Figure 1. All 10 knots transients are listed in table 1. Knot 2.6.2 corresponds to knot 6 in that table and it is the transient with the highest significance among them. It is also, the only transient that appears in Kelly et al. (2022). In addition, this knot has two additional counterimages in a triply-lensed young star cluster (family system 2.6). The two additional counterimages are indicated by red and blue arrows respectively. The fact that this transient is multiply-lensed, and one of its counterimages (knot 2.6.3) is also a transient, allowed us to examine if the variation detected is intrinsic by looking at its light curves, as the same variations would be seen in the lensed counterparts modulo a suitable time delay. In addition, the moderate magnification of these images can be used to set lower limits on the intrinsic luminosity of the young star cluster.

On the other hand, we can test whether stellar microlensing alone is sufficient to reproduce the detection rate of transients in the lensed young star clusters. Unlike caustic crossing events that feature individual stars being microlensed, the effect of microlensing on a group of stars as a whole is not well understood: Dai (2021) carried out the first and only calculation so far, showing star clusters (of Mass $\approx 10^{6-7} M_\odot$) could exhibit a very small level of flux variation (of the order of $\sim 1\%$) owing to microlensing; In our case, the estimated stellar mass of the young star clusters ($\sim 10^4 M_\odot$) in the Dragon Arc is orders of magnitude smaller than those consid-

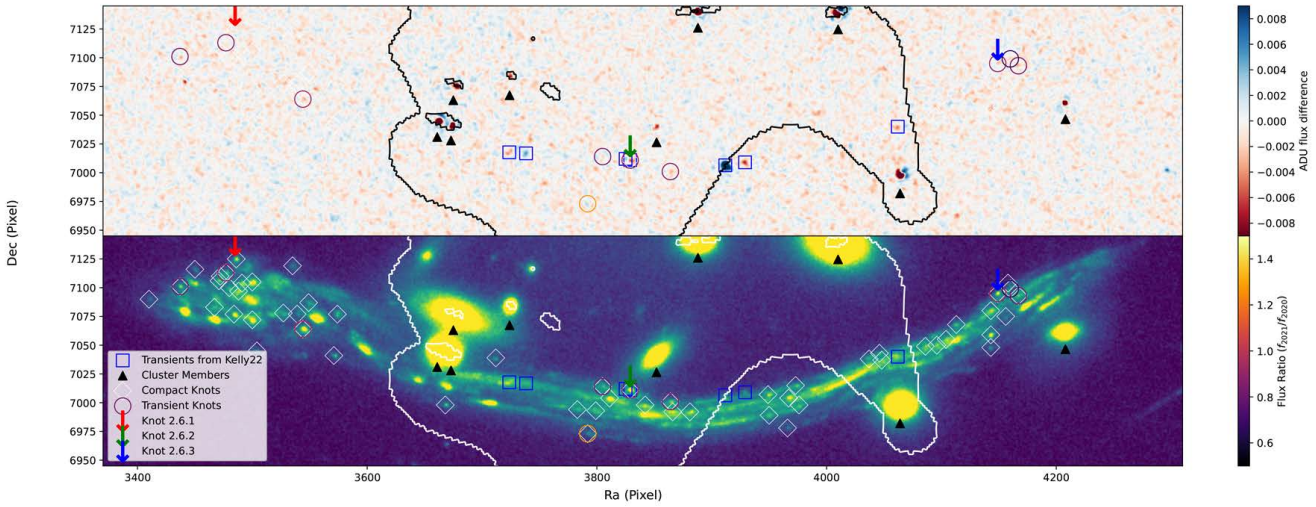

Figure 1. Image of Flashlights F200LP observation in 2021 subtracted by that in 2020 (upper panel) and Flashlights F200LP image in 2021 (lower panel). In both images, we show: The critical curve of our lens model as to be introduced in Section 3 (Black and White curves); The transients reported by Kelly et al. (2022) (Blue squares); The knots showing more than 3σ brightness variation between the two Flashlights observations (colored circle, which indicate the flux ratio in the lower color bar); All the knots that are considered as young star clusters based on our selection criteria in Section 5.3.2 (White diamonds). We specifically labeled the three multiply-lensed images in system 2.6, where two of them are classified as transients and thus used as a case study in this paper, with red, green, and blue arrows respectively. Notice that there are spots denoted with black triangles in the upper panel that are not recognized as transients despite the flux difference. Those are expected to be the photon noise fluctuation for the bright objects (see the corresponding position in the lower panel) within the FOV and thus are not genuine transients.

ered by Dai (2021). In this case, one expects the effect of microlensing to be more pronounced in a young star cluster because there are more young bright stars that dominate the total brightness – a microlensing event of one of these young bright stars can result in significant changes in the observed brightness. In this work, we use numerical simulations to address the flux variation in young star clusters due to microlensing.

This paper is organized as follows: We first introduce the data used in our work in Section 2, and the lens model constructed to understand the nature of transients in Section 3. With our lens model, we attempt to construct light curves and hence search for evidence of intrinsic variability in Section 4. Then, in Section 5, we describe our microlensing simulation and explore if stellar microlensing alone can explain all the observed lensed young star cluster transients. Finally, we discuss our various results in Section 6 and conclude in Section 7. Throughout this paper, we adopt magnitudes in the AB magnitude system (Oke & Gunn 1983), along with standard cosmological parameters: $\Omega_m = 0.3$, $\Omega_\Lambda = 0.7$ and $H_0 = 70$ km s^{-1}Mpc^{-1}.

2. DATA

2.1. *Flashlights*

As mentioned in Section 1, the Flashlights program targeted the six galaxy clusters observed in the HFF program by acquiring even deeper images of these clusters with the HST using the WFC3 in two filters, UVIS F200LP and UVIS F350LP, separated by about one year. Owing to a change in the initially proposed filters for the observations (from the ACS/WFC Clear to WFC3 UVIS F350LP), images of A370 were acquired in the UVIS F200LP filter only, taken on 2020 Feb 27 and 2021 Jan 22. Each image has an effective exposure time of 6.07 hours and reached a 5σ detection threshold of $m_{AB} = 30$ in individual pixels with a pixel size of 30 mas on a side. The F200LP filter spans the wavelength range 1990 Å to 10550 Å, spanning observed wavelengths from the UV to NIR – as we do not know a priori what color transients may have. The Flashlights images cover the same field of view (FOV) as the HFF observations of $\sim$7 arcmin^2.

2.2. *Hubble Frontier Fields*

Next to the Flashlights program, the deepest HST images of A370 were taken in the HFF program (Lotz et al. 2017). In the latter program, images were taken with the ACS camera in the F435W, F606W, and F814W filters, as well as with the WFC3 camera in the F105W, F125W, F140W, and F160W filters. Note that there is therefore no overlap in filter coverage between the HFF and Flashlights programs. The HFF images of A370 were taken between December 2015 and Febru-

ary 2016. Just like in the Flashlights program, A370 was observed at a common telescope roll angle in all the images taken for the HFF program. We used the final stacked images retrieved from the HFF archive (https://archive.stsci.edu/prepds/frontier/) for much of our work, although we also made images taken at individual epochs to measure the light curves described in Section 4. These images have a pixel size of 30 mas, the same pixel size as the images in the Flashlights program.

2.3. *Other HST Observations*

HST images of A370 also were acquired as part of the Beyond Ultra-deep Frontier Fields And Legacy Observations (BUFFALO; GO-15117) program. The BUFFALO observations of A370 comprise four exposures taken with both the F606W (∼20 min exposure per image) and F814W (∼10 min exposure per image) filters between 2018 Dec 19 and 2019 Jan 30, the last observation made just over a year before the beginning of the Flashlights observations of the same cluster (albeit in different filters). The FOV of the BUFFALO images of A370 is ∼36 arcmin^2, over five times larger than that of the HFF and Flashlights images. To produce images having the same pixel size as the Flashlights and HFF images, we re-calibrated the BUFFALO images, realigned them with TweakReg, and then resampled the images to a pixel size of 30 mas using AstroDrizzle. The BUFFALO images were used together with the HFF and Flashlights images to assemble the light curves described in Section 4.

2.4. *MUSE Spectra*

Reliable identifications of multiply-lensed counterparts along with accurate determinations of their redshifts are crucial starting points for constructing reliable lens models. Furthermore, the identification of cluster members is necessary to provide one of the ingredients for lens models of galaxy clusters. For these purposes, we used spectroscopic measurements for A370 from observations with the Multi Unit Spectroscopic Explorer (MUSE; Bacon et al. 2010) on the Very Large Telescope (VLT). MUSE is an integral field unit with a FOV of 1 arcmin^2, providing images with a pixel size of 0.2″ over the wavelength range 465 nm to 930 nm.

The latest release of the MUSE data for A370 covers a FOV of ∼4 arcmin^2 that is comparable to the estimated angular size of A370 (Lagattuta et al. 2019). Although smaller than the FOV of the aforementioned HST observations of A370, it is nevertheless sufficiently large to span the Einstein ring of the cluster and beyond – including the Dragon arc. Notice that the pixel size of the MUSE images (0.2″) is much larger than that of the HFF images (0.03″), in keeping with the much larger PSF of the MUSE images (∼0.8″) compared with the HST images. To remove as best as possible skylines, we applied ZAP (Soto et al. 2016) to the images after masking out cataloged sources.

3. LENS MODELING

The most recent lens models of A370 are those reported by Diego et al. (2018, hereafter D18) and Lagattuta et al. (2019, hereafter L19). In addition to a common subset of 30 multiply-lensed systems serving as constraints on their lens models, D18 also used two sets of multiply-lensed knots that they identified in the Dragon arc, whereas L19 also used 15 other multiply-lensed systems that they identified. In our work, we started with the same set of multiply-lensed systems identified by L19, comprising a total of 136 lensed images – but ended up combining two systems into one, as well as omitting another, for reasons explained in Section 3.2. Furthermore, to provide more accurate lensing predictions in the region of the Dragon Arc, we optimized our lens model over this region by using as additional constraints nine sets of multiply-lensed knots in the Dragon Arc. The manner by which these multiply-lensed knots were identified is described in Section 3.2.

3.1. *Ingredients*

Our lens model is composed of mass components representing the individual cluster members as well as those representing the cluster-scale DM halos. As previously found by L19, multiple cluster-scale DM halos are necessary to reproduce the multiply-lensed images generated by this dynamically disturbed cluster. We constructed our lens model using the lens modeling algorithm `Glafic` (Oguri 2010).

To select cluster members, we compiled a list of all galaxies lying in the redshift interval $z = 0.3745 \pm 0.0231$ (i.e., $\pm 3\sigma$ from the center of a Gaussian distribution in radial velocities; L19). Redshifts were taken from the spectroscopic redshift catalog compiled by Richard et al. (2021), all based on observations with MUSE. Out of a total of 222 galaxies that satisfied the selection criteria, we omitted 4 galaxies flagged as having poor photometric quality, thus leaving 218 spectroscopically-identified cluster members. In the lens modeling, we parameterized all the selected cluster members, apart from the two Brightest Cluster Galaxies (BCGs), using a modified Jaffe profile as described by Keeton (2001), with a truncation radius and mass scaled to their individual luminosities (following the same procedure as described in Chow et al. 2024). In the preliminary lens model, we forced all these cluster members to share the

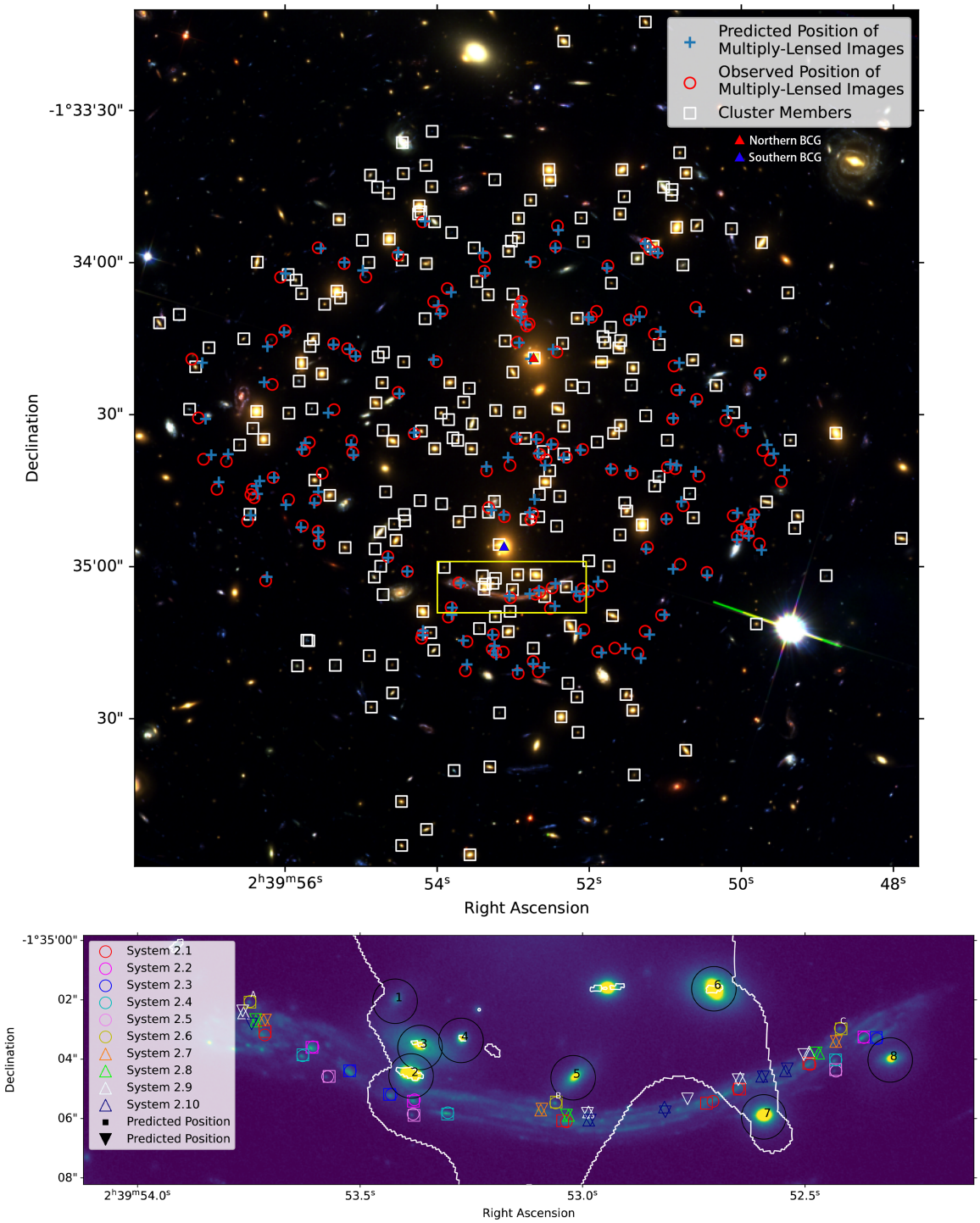

Figure 2. An RGB image of A370, composed of F435W (Blue), F606W (Green), and F814W (Red) filters, denoted with cluster members (white squares), multiply-lensed images (red circles) and the positions of the multiply-lensed images (blue crosses) predicted by our lens model. We also show an image cutout of the Dragon Arc in F200LP at the bottom. In the image cutout, we marked the cluster members listed in Table 2 with black apertures. Also, the observed positions of the multiply-lensed knots in the Dragon Arc are denoted with colored circles and triangles. The predicted positions of these knots are denoted with squares and inverted triangles, where the observed and predicted image positions of the same system have the same color. The white line overlaying on the images is the Critical Curve of the lens model at the redshift of the Dragon Arc ($z = 0.7251$). The counterimages of system 2.6 are highlighted with the middle yellow circle and labeled as A, B, and C respectively.

same mass-to-light ratios (M/L); when optimizing our lens model over the Dragon Arc, we allowed the eight

cluster members in the close vicinity (those enclosed by black ellipses in the bottom panel of Figure 2) to have varying M/L ratios. To parameterize the two BCGs, we adopted Sersic profiles, for which their M/L and Sersic indices were permitted to be independent of each other and to be freely solved. We allowed these freedoms as several multiply-lensed images lie in their close vicinity, thus placing more stringent constraints on their mass profiles. The centroid positions, ellipticities, and position angles of all these cluster members were taken from Richard et al. (2021).

Numerous studies suggest that A370 is likely to be in the midst of a merger between two (or more) galaxy clusters (e.g.: Oemler et al. 1997; Filippis et al. 2005; Richard et al. 2010; Strait et al. 2018; Molnar et al. 2020; Ghosh et al. 2021; de Oliveira et al. 2022). Thus motivated, we began by implementing into our lens model two cluster-scale Dark Matter haloes having NFW profiles (Navarro et al. 1997; Oguri 2021). In so doing, we found relatively large discrepancies between the predicted and observed positions among many of the multiply-lensed systems used as constraints. Adding one more Dark Matter halo, also having an NFW profile, significantly improved upon the agreement between the predicted and observed positions of the multiply-lensed systems. Adding yet another Dark Matter halo provided no improvement in agreement. Our lens model therefore comprises three Dark Matter halos, all having NFW profiles, for A370. For comparison, L19 incorporated four Dark Matter halos into their lens model.

To allow for the possibility of gravitational perturbations produced by an inhomogeneous distribution of matter around the cluster, we also explored whether including a shear term (Keeton et al. 1997) in our lens model improved the agreement between the predicted and observed positions of the multiply-lensed systems used as constraints. In the lens modeling, we allowed the strength of the shear (γ, the stretching power), convergence (κ), and shear angle to be freely solved. We found the best-fit lens model to require a shear term, for which the parameters of this model are listed in Table 2. The critical curve predicted by our lens model in the region of the Dragon Arc, for which our lens model is especially tuned, is shown by the white line in the bottom panel of Figure 2.

3.2. *Constraints*

To constrain our lens model, we employed nearly all the multiply-lensed images identified by L19, except for the following minor modifications:

1. Combined systems 7 and 10. Both D18 and L19 suspect, based on their lens models, that these two systems may actually be part of one system. Our lens model affirms systems 7 and 10 to be lensed counterparts, as is consistent with their common redshift of z = 2.7512 as determined from their MUSE spectra (Richard et al. 2021).

2. Omitted system 39. We failed to reproduce the proposed multiply-lensed counterparts of this system in any of our lens models. MUSE spectra show only the marginal detection of an emission line, if any, among the proposed multiply-lensed counterparts.

A complete list of the 43 multiply-lensed systems, which together form 133 lensed images, used to constrain our preliminary lens model (i.e., before being tuned over the Dragon arc) is compiled in Table 5 of the Appendix. Their image counterparts are enclosed within red circles in the upper panel of Figure 2; as can be seen, the multiply-lensed images are quite evenly distributed throughout the cluster. Our preliminary lens model constrained by just these systems is able to reproduce all their positions to within with a root-mean-square (rms) dispersion of $0\farcs88$, comparable to the rms positional dispersions of other models like that of L19. As a test of the predictability of our lens model, we were able to reproduce the observed flux ratios of systems 4, 9, and 26, the only systems for which we were able to extract reliable photometry (one or more lensed counterparts of the remaining systems lie close to cluster members or other bright objects), to within 3σ.

To optimize our lens model over the Dragon arc, we searched for additional multiply-lensed counterparts within the Dragon arc. As can be seen in the lower panel of Figure 2, the Dragon arc contains a multitude of knots, at least some of which correspond to young star clusters as we shall explain. We searched for multiply-lensed counterparts by looking for knots having similar colors, after which we checked their spectra from MUSE. As an additional check, we delensed and released the knots thus selected to verify that they are indeed associated based on the predicted positions of their lensed counterparts. In this way, we identified five sets of multiply-lensed knots having different colors, all of which are relatively blue compared to the more diffuse arcs in which they are embedded, as well as bright emission lines characteristic of H II regions; the spectra of all these knots are shown in Figure 12 of the Appendix. We refer to these five sets of multiply-lensed knots as systems 2.2 to 2.6; system 2.1 having already been identified in previous studies as the relatively red bulge of

Table 2. Best-fit Model Parameters

Component (Profile)	$\Delta\alpha('')$	$\Delta\delta('')$	e	θ (deg)	Mass ($M_\odot h^{-1}$)	c (NFW)/ n (Sersic)	$r_{\rm trun}$ ($''$, Sersic)
DM1 (NFW)	-0.01	5.40	0.20	-174.73	1.06×10^{15}	5.11	–
DM2 (NFW)	27.69	40.22	0.64	-7.11	9.01×10^{14}	0.28	–
DM3 (NFW)	-5.25	36.58	0.32	-160.29	1.24×10^{14}	7.68	–
NBCG (Sersic)	-5.90	37.24	0.20	357.31	4.05×10^{11}	4.34	6.36
SBCG (Sersic)	0.01	0.02	0.30	315.12	3.64×10^{11}	5.18	3.55
Cluster Members	–	–	–	–	$\sigma_* = 258.32$	–	$r_{\rm trun,*} = 34.10$
Shear	–	–	–	-43.40	–	γ = 3.47e-2	–
Cluster Member 1	-4.44	-5.73	0.59	-51.93	1.20×10^{10}	–	1.0
Cluster Member 2	-3.99	-8.35	0.30	68.17	1.75×10^{11}	–	2.0
Cluster Member 3	-3.74	-7.35	0.72	69.52	1.28×10^{11}	–	5.6
Cluster Member 4	-2.23	-7.17	0.12	-14.29	2.00×10^{11}	–	13.7
Cluster Member 5	1.62	-8.43	0.48	-49.95	8.34×10^{10}	–	2.0
Cluster Member 6	6.26	-5.51	0.34	71.95	1.41×10^{12}	–	21.1
Cluster Member 7	7.95	-9.79	0.13	75.52	9.65×10^{11}	–	18.3
Cluster Member 8	12.24	-7.89	0.23	-58.59	1.21×10^{11}	–	9.1

NOTE—(1)$\Delta\alpha('')$ and $\Delta\delta('')$ are relative to the reference coordinate ($\alpha = 39.97134$, $\delta = -1.5822597$). (2) Angles are anti-clockwise from Up North. (3) σ_* and $r_{\rm trun,*}$ denote the velocity dispersion and radius of the brightest non-BCG cluster member respectively, such that the respective values of any cluster member scales with their brightness compared with that of the brightest non-BCG cluster member.

the galaxy that is multiply-lensed to form the Dragon arc, and which was used as one of the lensing constraints in our preliminary lens model. Note that D19 had previously also identified the same lensed counterparts for systems 2.2 and 2.3, but without the benefit of spectroscopy, providing further reassurance that these systems have been correctly identified. The lensed counterparts of all these systems are enclosed within color circles in the lower panel of Figure 2. Using systems 2.1–2.6 in addition to the lensed counterparts belonging to the other systems mentioned above, we solved for a new lens model that is now especially tuned over the Dragon arc.

We used the newly tuned lens model to search for even dimmer (and therefore less obvious) lensed counterparts in the Dragon arc. To make this possible, we first created an unsharp-masked image of the Dragon arc, and then delensing and relensing selected knots to predict the positions of their lensed counterparts. In this way, we identified four more sets of multiply-lensed counterparts labeled as systems 2.7–2.10, which are enclosed within triangles in the lower panel of Figure 2. Unfortunately, all of these proposed lensed counterparts are too dim to display useful spectra from MUSE. Nonetheless, all are presumably star clusters.

The positions of all the lensed counterparts in systems 2.2–2.10, as well as system 2.1 for the sake of completeness (also listed in Table 5), are compiled in Table 3. All these systems, along with the other multiply-lensed systems compiled in Table 5, are used to constrain our final lens model for A370 – which is therefore optimized over the Dragon arc. This lens model is able to reproduce the positions of all the multiply-lensed knots in the Dragon Arc used as constraints with an rms dispersion of $0.07''$, which is comparable with the typical size of the PSF (FWHM $\approx 0.08''$) of the HFF images.

Table 3. Relative positions of the counterimages of knots in the Dragon Arc

Image	$\Delta\alpha('')$	$\Delta\delta('')$	Image	$\Delta\alpha('')$	$\Delta\delta('')$
2.1.1	8.96	-7.08	2.6.1	9.45	-5.96
2.1.2	-1.20	-10.01	**2.6.2**	-0.84	-9.38
2.1.3	-6.14	-9.32	**2.6.3**	-10.43	-6.86
2.1.4	-6.99	-8.90	2.7.1	9.00	-6.57
2.1.5	-9.41	-8.08	2.7.2	-0.34	-9.62
2.2.1	7.34	-7.49	2.7.3	-10.27	-7.30
2.2.2	3.92	-9.27	2.8.1	9.26	-6.34
2.2.3	-11.22	-7.17	2.8.2	-1.13	-9.80
2.3.1	6.08	-8.30	2.8.3	-9.70	-7.70
2.3.2	4.70	-9.09	2.9.1	9.68	-6.34
2.3.3	-11.67	-7.21	2.9.2	-1.95	-9.68
2.4.1	7.68	-7.79	2.9.3	-7.06	-8.53
2.4.2	2.79	-9.71	2.9.4	-9.38	-7.66
2.4.3	-10.28	-7.93	2.10.1	-1.95	-9.96
2.5.1	6.84	-8.49	2.10.2	-4.50	-9.51
2.5.2	3.96	-9.75	2.10.3	-7.78	-8.48
2.5.3	-10.28	-8.30	2.10.4	-8.58	-8.29

NOTE—(1) $\Delta\alpha('')$ and $\Delta\delta('')$ are relative to the reference coordinate ($\alpha = 39.97134$, $\delta = -1.5822597$). (2) Knots in bold text demonstrate $\geq 3\sigma$ brightness variation between the two Flashlights Epochs

4. INTRINSIC VARIABILITY?

Among the many transients detected in the region of the Dragon arc as shown in Figure 1, two coincide with system 2.6. In this system, both knots 2.6.2 and 2.6.3 dimmed at comparable levels ($\Delta m = 0.16 \pm 0.02$ for knot 2.6.2, and $\Delta m = 0.09 \pm 0.02$ for knot 2.6.3) between the two epochs of the Flashlights observations separated by nearly one year – raising the possibility that their changes in brightness are intrinsic to the source. Such an intrinsic brightness change is possible if, for instance, a Luminous Blue Variable (LBV) in the young star cluster corresponding to system 2.6 was caught in the decay phase of an outburst.

If the dimming of knots 2.6.2 and 2.6.3 is intrinsic to system 2.6, the lack of a similar brightness change in knot 2.6.1 would then require light from this knot to arrive at a much different time (either earlier or later) than knots 2.6.2 and 2.6.3. To test this possibility, we examine differences in the arrival time of light from knots 2.6.1–2.6.3 as predicted by our lens model: if the light variation is intrinsic to the source, we should see the same brightness change in all the lensed counterparts subject to a time delay. Our lens model predicts light from knot 2.6.3 to arrive ∼178 days earlier than knot 2.6.2, whereas light from knot 2.6.1 to have arrived even earlier: ∼107 days earlier than knot 2.6.3, and ∼285 days earlier than knot 2.6.2. Thus, an event that occurred in system 2.6 would be seen first in knot 2.6.2 before knot 2.6.3, and thereafter followed by knot 2.6.1. Given that the separation between the two epochs of Flashlight observations is ∼ 330 days, knot 2.6.1 should therefore have dimmed between the two epochs of the Flashlight observations – provided that system 2.6 had undergone a gradual dimming throughout all the epochs in which its three multiply-lensed knots were observed in the Flashlights program.

4.1. *Light Curves*

We construct a light curve for system 2.6 by taking the aforementioned time delays into consideration, as well as correcting for the lensing magnifications of the individual knots in this system as predicted by our lens model. The result is shown is shown in Figure 3*a*. As can be seen, the light curve of this system displays a more complex time behavior than just a simple dimming, perhaps, therefore, explaining the lack of any detectable brightness change in knot 2.6.1.

Before drawing any further inferences from the light curve of Figure 3*a*, it is prudent to construct light curves for the other knots in the Dragon arc to check on the reliability of their inferred lensing magnifications – as even relatively small errors in the inferred lensing magnifications of different counterparts belonging to the same

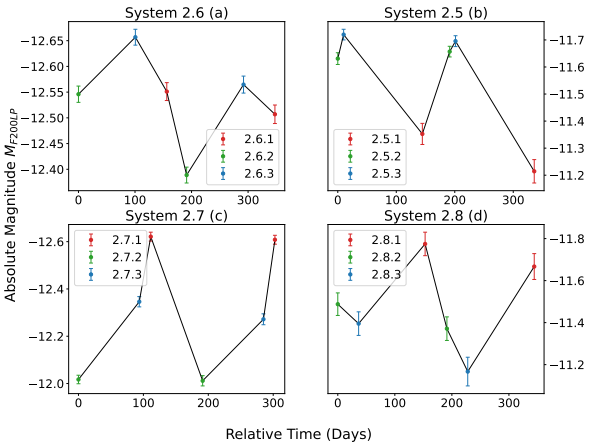

Figure 3. The light curves of Multiply-Lensed Systems 2.5 to 2.8 constructed with the two Flashlights observations, corrected by the lensing magnification predicted by our lens model. For each of the systems, photometry with the same color means that they are from the same counterimage as denoted in the legend, but at two different Flashlights observations.

system can give rise to apparent time variability in their light curves constructed in the manner described above. In Figure 3*b*–*d*, we show the light curves constructed for systems 2.5, 2.7, and 2.8, all selected for their similar lensing configurations to system 2.6. Although none of the lensed counterparts in these systems display any significant changes in brightness between the two Flashlights epochs, nonetheless their light curves display a similar level of variability as system 2.6. Their apparent time variability is therefore induced solely by corrections applied to their individual lensing magnifications as predicted by our lens model, rather than any real time variability in the brightnesses of these systems. Errors in the inferred lensing magnification of individual counterparts could arise from systematic errors in our lens model, or the presence of other lensing objects not taken into account in our lens model (e.g., intracluster globular clusters; see Diego 2024). At the accuracy of lensing magnifications predicted by our lens model for A370, a conclusive test of intrinsic variability would require observations over multiple (much more than two) epochs spanning a longer period, so as to test whether changes in the brightness of a given lensed counterpart are reflected in the other lensed counterparts with a suitable time delay.

Although the available data do not allow the aforementioned test, we can check for other examples of time variability from the HFF observations of A370, comprising observations at multiple epochs spanning about 2 months. As mentioned in Section 2, these observations

were made about 4–5 yr earlier than those in the Flashlights program. Figure 5 shows the light curves for the individual knots in system 2.6 in the F435W, F606W, and F814W filters, for which observations were made with relatively even time cadence. Despite the individual images being much shallow than those taken in the Flashlights program, we find instances during which the brightness of a given knot either increased or decreased by $> 3\sigma$ between one epoch and a later epoch; e.g., knot 2.6.2 between MJD 57377 and 57389 in F814W, and knot 2.6.3 between MJD 57385 and MJD 57404 in F814W. We show the respective images in Figure 4, as well as the difference in images between the epochs to demonstrate the change in brightness therein. As the time span of the HFF observations is much shorter than the time delay between the arrival of light from knots 2.6.2 and 2.6.3, changes in their brightnesses during the HFF observations must therefore correspond to different events (or different intervals of the same event). Interestingly, the maximal change in brightnesses of both these knots of $\sim$0.2 mag is comparable to the change in brightnesses observed for the same two knots between the two epochs of the Flashlights observations. Furthermore, only significant changes in brightness were observed for knots 2.6.2 and 2.6.3, whereas knot 2.6.1 showed no statistically significant changes in brightness over the entire duration of the HFF observations.

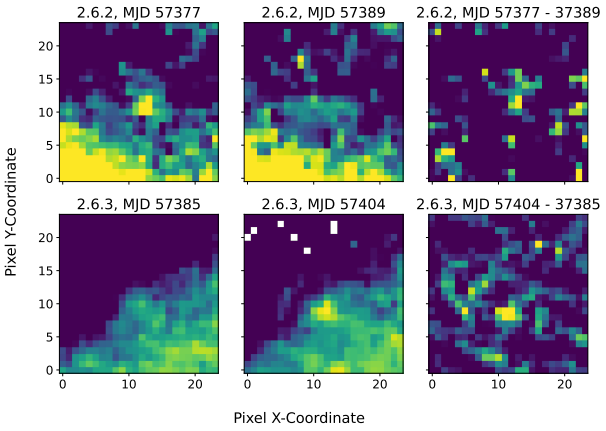

Figure 4. The individual F814W HFF images of knot 2.6.2 (Top Row) and knot 2.6.3 (Bottom Row), on epochs where their brightnesses differ by more than 3σ (Left and Middle Column). In the Right Column, we show the subtraction between the two images on the Left and Middle columns (the image with a brighter knot subtracted by the image with a dimmer knot) to demonstrate the change in brightness. The images are in arbitrary scaling to better illustrate the changes.

As one final test of intrinsic variability, we checked whether variations in brightness are accompanied also by variations in color. As lensing does not change color, any changes in color would immediately reveal intrinsic variability. We find no significant changes in color in any episodes in which we see significant changes in brightness, either in the HFF or Flashlights program, thus providing no firm evidence for (albeit not ruling out) intrinsic variability.

5. EXTRINSIC VARIABILITY

In this section, we explore whether the observed brightness variations of either singly- or multiply-lensed star clusters in the Dragon arc, as shown in Figure 1, might be imposed by objects external to these star clusters. Specifically, we examine whether their brightness variations could be induced through microlensing by relatively compact objects having stellar masses at the redshift of the galaxy cluster A370. Such objects – whether they be intracluster stars or primordial black holes – located along the sightline to a background star cluster can alter (either increasing or decreasing) the brightness of individual stars in the star cluster, thus also altering the observed total brightness of the entire star cluster. As the foreground lensing objects move across the sky relative to the background star clusters, the observed total brightness of these star clusters can vary with time – thus appearing as lensed transients.

To explore the level of extrinsic variability induced by microlensing, it is more convenient to consider what happens in the source plane; i.e., at the redshift of the galaxy that is multiply-lensed to form the Dragon arc. In this plane, each microlens (at the redshift of A370) produces a microcaustic; the motion of a microlens across a background star cluster is then equivalent to the motion of its microcaustic through this star cluster. In Section 5.1, we present our microlensing simulations involving the motion of a web of microcaustics through a stellar population. From these simulations, we derive a semi-analytical approximation of the resulting change in the total brightness of this stellar population, as described in Section 5.2. In Section 5.3, we then consider whether our model predictions can explain the rate of transients observed in the Dragon arc at their observed changes in brightnesses.

5.1. *Microlensing Simulation*

Figure 6 shows a small region of our simulation area, over which the lensing magnification imposed on a star cluster is indicated in greyscale. The lensing magnification over this area is composed of a macro-magnification imposed by the galaxy cluster (the macrolens, as described by the lens model derived in Section 3), which imposes an essentially constant magnification over a

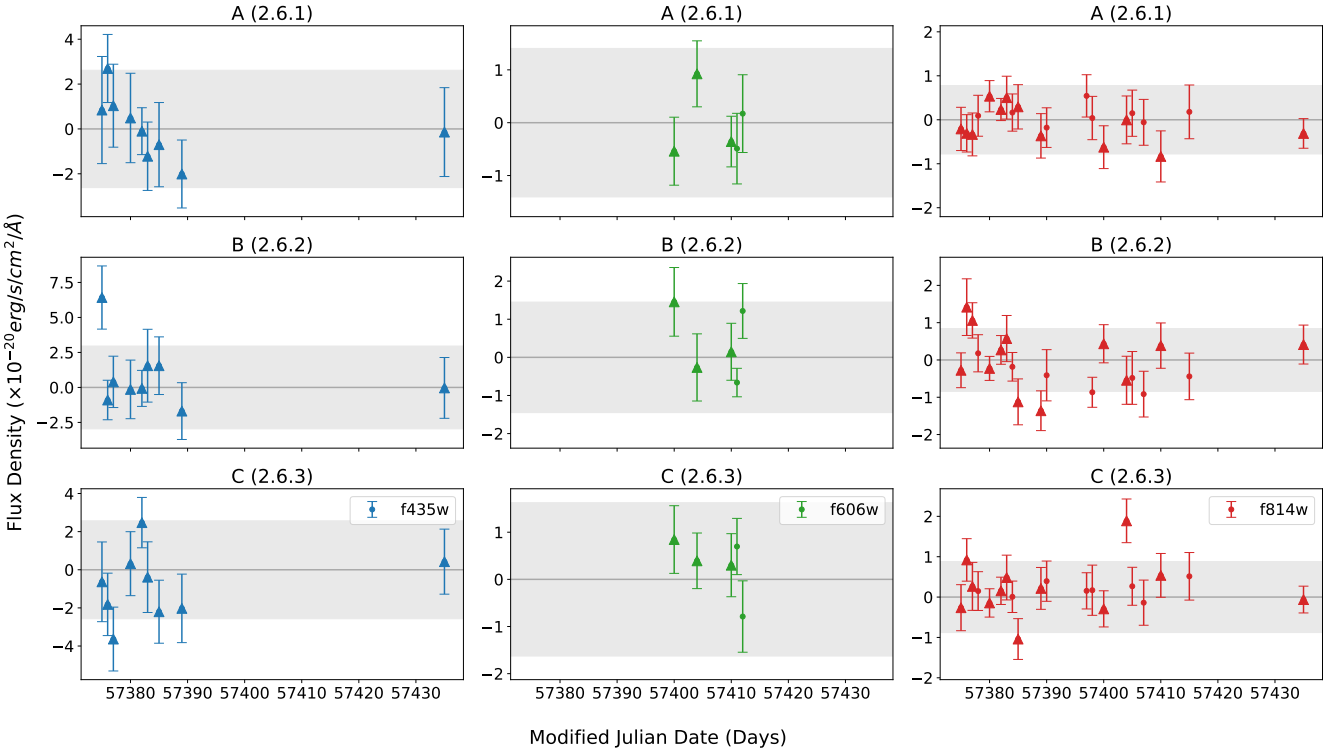

Figure 5. The light curves of the three counterimages of system 2.6 constructed with individual HFF observations in three optical filters (F435W, F606W, and F814W). The light curves are in order from the top to the bottom panel: Top (A, 2.6.1), middle (B, 2.6.2), and bottom (C, 2.6.3) counterimage, and from left to right column: left (F435W), middle (F606W), right (F814W). We indicate observations carried out with two or more filters simultaneously in a day with a triangle marker. Moreover, we add a line at $y = 0$ (brightness in co-add image) for reference, where the gray shaded band represents the $\pm 1.5\sigma$ of the mean uncertainty of the flux differences in each epoch so the thickness of the band is 3σ – if any of the data pairs lie beyond two sides of the gray band, the pairs show flux variation that is more than 3σ.

background star cluster, as well as a web of micro-magnifications imposed by a collection of microlenses. The latter can dramatically decrease or increase the lensing magnification imposed by the macrolens, thus creating localized regions of dark and white features in the magnification map that each corresponds to a microcaustic (associated with an individual microlens). The typical scale of a microcaustic is a few thousand AU, and therefore orders of magnitude smaller than the typical size of a star cluster.

The color dots in Figure 6 represent stars that have been randomly distributed over the simulation area. The two different colors indicate their positions as observed at two different epochs owing to their motion relative to the microcaustics (in this case, from the blue to the red positions over time). Their shifts in positions correspond to an assumed bulk velocity of 1000 km s^{-1} between the stars and the web of microcaustics (see details in Section 5.1.3). At this velocity, a given star moves by 210 AU relative to the microcaustics in one year (or 190 AU between the two Flashlights observations separated by slightly less than a year). As can be seen, although the maco-magnification is constant over the simulation area, the motion of individual stars relative to the individual microcaustics can dramatically change the brightness of individual stars – and in this way potentially change the collective brightness of the star cluster, thus seen as a lensed transient.

In summary, our simulation is therefore composed of four components: (i) the macrolens that contribute a constant magnification over the simulated region corresponding to an individual background star cluster; (ii) a collection of microlenses, which is characterized by their abundance or surface mass density; (iii) the mass (and therefore luminosity) function of the stellar population corresponding to the background star cluster; and (iv) a relative displacement between the stellar population and the web of microcaustics representing observations at two different epochs. To understand how the individual components affect the result of our simulations, we explored a range of simulation parameters. In the following subsections, the parameters of each component are described in more detail.

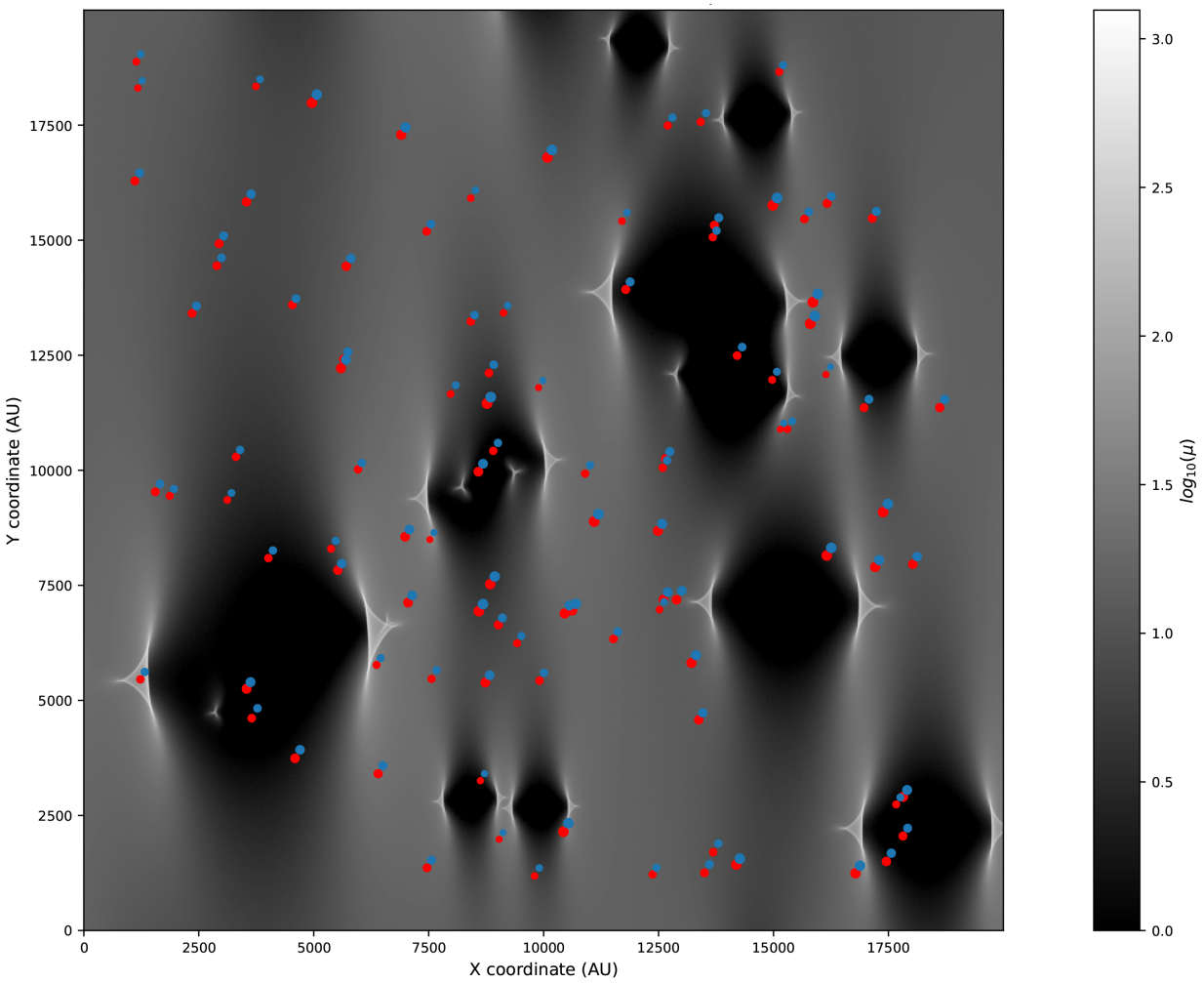

Figure 6. A stellar population (dots) sprinkled on a field of microcaustics (greyscale). For this simulation, the surface mass density of microlenses is $50\,M_\odot\,\mathrm{pc}^{-2}$ and the macro-magnification is -13.5. Red dots represent a star at a random position, while blue dots are the same star but ~ 1 year after (assuming a relative velocity of 1000 km s^{-1}). The (bulk) direction of motion is fixed for all the stars at $\sim 30^\circ$ clockwise from the y-axis. This illustration shows only a small portion of the full FOV which is ~ 5 times larger.

5.1.1. *Microcaustics*

In galaxy clusters, microlensing can be induced by intracluster stars or, in the situation considered here, stars at the outskirts of cluster members. In either case, the stars involved are relatively old and therefore have relatively low masses. We assume that these stars have a mass function described by a Kroupa initial mass function (IMF) (Kroupa 2001) that is truncated at $M_\odot = 1.4M_\odot$, corresponding to the upper mass threshold for F-type stars. Based on an analysis of the intracluster light performed by Morishita et al. (2017), we estimate the surface mass density of intra-cluster stars in the vicinity of the Dragon Arc to be $\sim 10M_\odot/\mathrm{pc}^2$ (equivalent to $\kappa_\star \approx 0.003$). Knot 2.6.2 is located especially close to a cluster member (see Figure 2), which makes a significant contribution to the stellar surface density at the position of this knot. We compute a contribution from this cluster member of $\sim 40M_\odot/\mathrm{pc}^2$ (equivalent to $\kappa_\star \approx 0.011$), and therefore a total stellar surface mass density at the position of knot 2.6.2 to be $\sim 50M_\odot/\mathrm{pc}^2$ (equivalent to $\kappa_\star \approx 0.014$). Details of this computation can be found in the Appendix.

On top of stellar microlenses, we also explore whether the addition of primordial black holes (PBHs) can better explain the observed transient rate among star clusters in the Dragon arc. In our simulation, we consider PBHs having identical masses of $30M_\odot$, as is motivated by the LIGO detection of a merger event that indicates the

Table 4. Tested Simulation Parameters

Surface Mass Density, $\kappa_\star$	Macro-Magnification, μ	Relative Displacement, D (AU)	30 $M_\odot$ PBH fraction in DM, $f(M)$
		20	
0.005	-7	100	0
		190*	
0.014*	-13.5*	400	
		600	1.5% ($\kappa_\star = 0.012$)
0.02	-27	1000	

NOTE—* Denotes parameters that represent the physical scenario of knot 2.6.2 observed by the two Flashlights Epochs

possible existence of PBHs with such masses (Abbott et al. 2016; Bird et al. 2016). The result of our simulation, however, is not dependent on the exact mass of the PBHs within the range of order $\mathcal{O}(0.1-10)M_\odot$.

In each simulation run, we sample microlenses – stars alone, or both stars and PBHs – having a given surface mass density or combination of surface mass densities. These microlenses generate micro-critical curves on top of the macro magnification, μ (as given by our lens model for A370), in the image plane (at the redshift, $z = 0.375$, of the galaxy cluster). When projected back to the source place (at the redshift, $z = 0.7251$, of the multiply-lensed galaxy that constitutes the Dragon arc) via the lens equation, these microlenses generate a web of microcaustics as shown in Figure 6. In our simulations, we use a pixel size of 1 AU on a side in our computation box, driven by the need to well separate lensed stars belonging to star clusters in the Dragon arc, as well as to resolve changes in their positions between the two epochs of the Flashlight observations of A370 (owing to the motion of the lensed stars relative to the microcaustics). This pixel size also ensures that each microcaustic (whether generated by stars or PBHs in the foreground cluster) is very well resolved, as can be visually appreciated from Figure 6. Our computation box has a size of 0.8 pc $\times$ 0.8 pc, in which we randomly distribute stellar microlenses having a number distribution with mass (i.e., mass function) drawn randomly from a Kroupa IMF truncated at 1.4 $M_\odot$. For a surface mass density of $50 M_\odot/\mathrm{pc}^2$ (equivalent to $\kappa_\star = 0.014$), our computation box would therefore contain ~ 100 stellar microlenses, ensuring a sampling in their mass function that is reflective of the adopted mass function given the relatively narrow mass range considered for these stars.

5.1.2. *Background Stellar Population*

The lensed star clusters in the Dragon arc under consideration all have similar colors and SEDs, display emission lines, have rather similar macro magnifications according to our macrolens model, and have rather similar apparent brightnesses. For simplicity, we therefore assume that all these star clusters have similar properties and, most importantly the same stellar luminosity function. Taking system 2.6.2 as being representative of these star clusters, we fitted a single stellar population to the SED of each of its lensed counterparts using `Bagpipes` (Carnall et al. 2018). The best-fit model, for which we assume no dust extinction, is for a stellar population having an age of $\sim$4 Myr and a total stellar mass $\sim 10^{4.4}\, M_\odot$ (with a poorly constrained metallicity). The estimated age is comparable to and the estimated total stellar mass nearly equal to the lower end of total stellar mass estimates for Westerlund 1, the most massive star cluster known in our Galaxy, with an estimated mass spanning the range $\sim 10^{4.7}$–$10^{5.0}\, M_\odot$ (see Negueruela et al. 2022, and references therein). At such a young age, even relatively massive stars (late-0 and later spectral types) would still be on the main sequence, as is required to produce an H II region detectable in emission lines.

As a starting point in our simulations, we assume a mass function for the lensed stars corresponding to a Kroupa IMF truncated at a mass of 100 $M_\odot$, and covert their mass to luminosity using the prescription in Duric (2004). As might be anticipated, and as we indeed find, any changes in the total brightness of a lensed star cluster between two epochs – owing to changes in the positions of lensed stars relative to microcaustics – are dominated by the most luminous stars (which contribute disproportionately to the luminosity of a star cluster). In the Appendix, we truncate the mass function of the lensed stars at 5 $M_\odot$ (corresponding to mid-B stars) to investigate the consequence of a possible overrepresentation of luminous stars in our starting simulations. Not surprisingly, the results differ for the two different upper limits in masses and therefore luminosities adopted for the lensed stars, but not by very much when considering only two observations separated by somewhat less than a year (as is the case for the Flashlights observations of A370). When considering longer timescales, however, the results become increasingly divergent for the two mass cutoffs, as might be anticipated

owing to a larger displacement between the lensed stars and microcaustics over a longer time interval.

As mentioned above, our computation box has a size of 0.8 pc × 0.8 pc, which is much smaller than the sizes of star-forming regions in our Galaxy having comparable total stellar masses (e.g., Westerlund 1, with an effective radius estimated at ∼3.7 pc; Negueruela et al. 2022). The size of our computation box is limited by the need to provide very high angular resolutions (pixel size of 1 AU) so as to separate individual lensed stars as well as the displacement of these stars relative to the microcaustics owing to their relative motion separated by about a year, while maintaining a manageable computational time. A single simulation of an entire star cluster would therefore require multiple computational boxes depending on the assumed sizes of the star clusters under consideration. Recall from Section 5.1.1 that the computational box contains ∼100 stellar microlenses (depending on the surface mass density of intracluster stars under consideration) distributed at random over the computation box, and having a mass function drawn randomly from a Kroupa IMF truncated at 1.4 $M_\odot$. As the pattern of microcaustics in this computation box is representative of that in any other (indeed, this consideration is the main constraint on the minimal size of a computation box, as explored in more detail in the Appendix), rather than using multiple computation boxes (with a statistically similar pattern of microcaustics) for a single simulation of an entire star cluster, we simply place all the stars in the star cluster into one computation box; i.e., this approach being equivalent to combining (imagine superposing) multiple computation boxes, so long as the web of microcaustics in the combined computation box is representative of any single computation box. This approach naturally also lightens the computation load.

For a total stellar mass for the lensed star cluster of $10^{4.4}\,M_\odot$ and a mass function corresponding to a Kroupa IMF truncated at $100\,M_\odot$, the total number of lensed stars in each computation box is therefore 54,000. In each simulation, we distribute these stars randomly over the computation box, and imposed a mass function drawn randomly from a Kroupa IMF truncated at $100\,M_\odot$ (for which we draw a total of 5,000 samplings in mass functions); to simulate their motion relative to the microcaustics as observed at two different epochs, all the stars are displaced by the same distance and at the same position angle (see Figure 6). In this way, we performed 50,000 such simulations (i.e, using each of the 5,000 samplings in mass functions ten times), with the lensed stars being displaced by the same distance but at a randomly selected position angle in each simulation. To check whether we properly sample the most luminous stars, we find that every sampling in mass function (and hence every simulation) contains at least one star having a mass of $\geq 80\,M_\odot$, sometimes as many as twelve such stars, with a median number of three such stars among all these samples.

5.1.3. *Relative Displacement*

The relative motion between the observer, microlenses (intracluster stars) contained within the macrolens (A370), and source (star clusters hosted by the multiply-lensed galaxy that forms the Dragon arc) can cause a change in the total brightness of the source owing to changes in the microlensing magnification of its individual stars. To assess the relative displacement between the microlenses and the source over a given time interval, we need to consider the relative transverse velocity involving the planes of the observer, lens, and source. By taking into account factors including the peculiar velocity of the Earth and the host galaxy, the velocity dispersion of a merging galaxy cluster, and the motion of young star clusters with respect to their host galaxy, the relative transverse velocity is approximately $1000\,\mathrm{km\ s^{-1}}$ (Kelly et al. 2018). For a time interval of 330 days between the two epochs of the Flashlights observations of A370, this relative transverse velocity translates to an observed transverse displacement of ∼190 AU between the plane of the lens and the source. Note that we have neglected the velocity dispersion of stars in the star cluster, for which the approximate velocity dispersion (given the inferred total stellar mass) is ∼2 orders of magnitude smaller than the bulk velocity assumed above.

As mentioned in Section 5.1.2, we displace the lensed stars along different (randomly selected) directions in different simulations, as we lack information on the angle of motion relative to the shear angle of the macrolens. Dai (2021) has shown that varying the angle of motion relative to this shear angle does not significantly affect the brightness variation of a star cluster owing to microlensing.

5.2. *Semi-Analytical Approximation of Simulation Result*

Figure 7 shows the probability distribution of brightness changes predicted for knot 2.6.2, one of the lensed counterparts of a multiply-lensed star cluster in the Dragon arc, as observed at two epochs separated by nearly 1 yr (specifically, 330 days). As explained in Section 5.1.2, this probability density is derived from 50,000 simulations in which the positions of lensed background stars are displaced relative to a web of microcaustics – generated by intracluster stars with a surface mass

density commensurate to that estimated at the position of knot 2.6.2 (see Section 5.1.1) – resulting in changes in the brightness of individual stars in a star cluster. These individual changes can add up to a change in the total brightness of a lensed star cluster, especially when relatively scarce luminous stars experience relatively large changes in micro-magnifications.

We find from Figure 7 that, most frequently, the cumulative effect of microlensing by intracluster stars results in no change (or imperceptible changes) to the total brightness of a star cluster between one epoch and another separated by the time interval considered. This result aligns with expectations that, most often, increases in micro-magnifications for some stars are counterbalanced by decreases in micro-magnifications for other stars, consistent with the findings by Dai (2021). Less frequently, this counteraction does not completely balance, resulting in small changes – either an increase or a decrease – in the total brightness of a star cluster. Much more rarely, one or more luminous stars experience an especially large change in micro-magnification owing to changes in their positions relative to the microcaustics, therefore producing a correspondingly large change in the total brightness of a star cluster.

To obtain a useful semi-analytical approximation to the results, we fit a Lorentzian function to the probability distribution shown in Figure 7 as given by the equation:

$$f(x;\, x_0, \sigma_L) = \frac{1}{\pi}\left(\frac{\sigma_L}{(x-x_0)^2+\sigma_L^2}\right), \qquad (1)$$

where x is the total brightness of the star cluster, x_0 its average brightness (i.e., total brightness in the absence of micro-lensing, subject only to macro-magnification), and σ_L the scale parameter (i.e., half-width at half-maximum, HWHM) of the Lorentzian function. In this way, the probability of seeing a change in total brightness by an amount corresponding to a factor $x : x_0$ can be simply calculated provided knowledge of σ_L. The best-fit Lorentzian function to the probability density shown in Figure 7 is indicated by an orange curve.

In the upper row of Figure 8, we show how σ_L changes with the (tangential) displacement, D, between stars and the microcaustics (lower x-axis) or, equivalently, the time interval between observations (upper x-axis). The different color points show how our simulations predict σ_L to change for different surface mass densities of intracluster stars, $\Sigma_\star$, at a given macro-magnification (left panel), or for different macro-magnifications, μ, at a given $\Sigma_\star$ (right panel). As might be anticipated, σ_L becomes larger (the Lorentzian function broader) as D increases, reflecting a larger possible change in the micro-magnification of individual stars for a larger change in their positions relative to the microcaustics. σ_L also becomes larger as μ increases, as a given fractional change in micro-magnification corresponds to a larger fractional change in stellar brightness for stars subject to larger macro-magnifications. The dependence of σ_L with either $\Sigma_\star$ or μ can be well approximated by Sigmoid functions, as indicated by the corresponding color curves, as expressed by the equation:

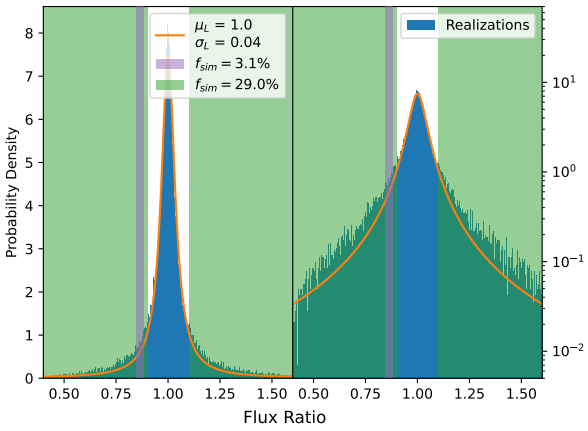

Figure 7. The distribution of the flux ratio from the 50,000 microlensing realizations. In all realizations, we assumed a stellar surface mass density of $\Sigma_\star = 50 M_\odot/pc^2$ ($\kappa_\star = 0.014$), a macro magnification of -13.5 and a relative displacement of $\sim$ 190AU. We have fitted a Lorentzian profile to the distribution, with the mean $x_0 = 1$ and scale parameter $\sigma_L = 0.04$. The right-hand side shows the same distribution but in a logarithmic scale, to better appreciate the tails of the Lorentzian distribution. The green bands illustrate the fractional change in flux ratio that exceeds 10% – the number of realizations falling within the green bands is 14,477, translating to a transient detection probability of 29.0% as indicated in the legend; The purple band shows the observed flux ratio ($\pm 1\sigma$ uncertainty) of knot 2.6.2, where 1550 realizations fall within the purple band, equivalent to a probability of 3.1%.

$$\sigma_L \approx \frac{D}{K_L + a_L D}, \quad D > 0\ , \qquad (2)$$

where K_L and a_L are the two constants of the Sigmoid functions.

In the lower row of Figure 8, we show how the probability of a total brightness change equal to or larger than 10% of the mean, $p(|\Delta f| \geq 10\%)$, depends on D for different $\Sigma_\star$ at a given μ (left panel), or for different μ at a given $\Sigma_\star$ (right panel). As might be anticipated, this probability becomes larger for a larger change in the positions of stars relative to the microcaustics, but up to a limit – as the displacement approaches the typical separation between microcaustics, this probability approaches a constant value. Just like in the upper row of

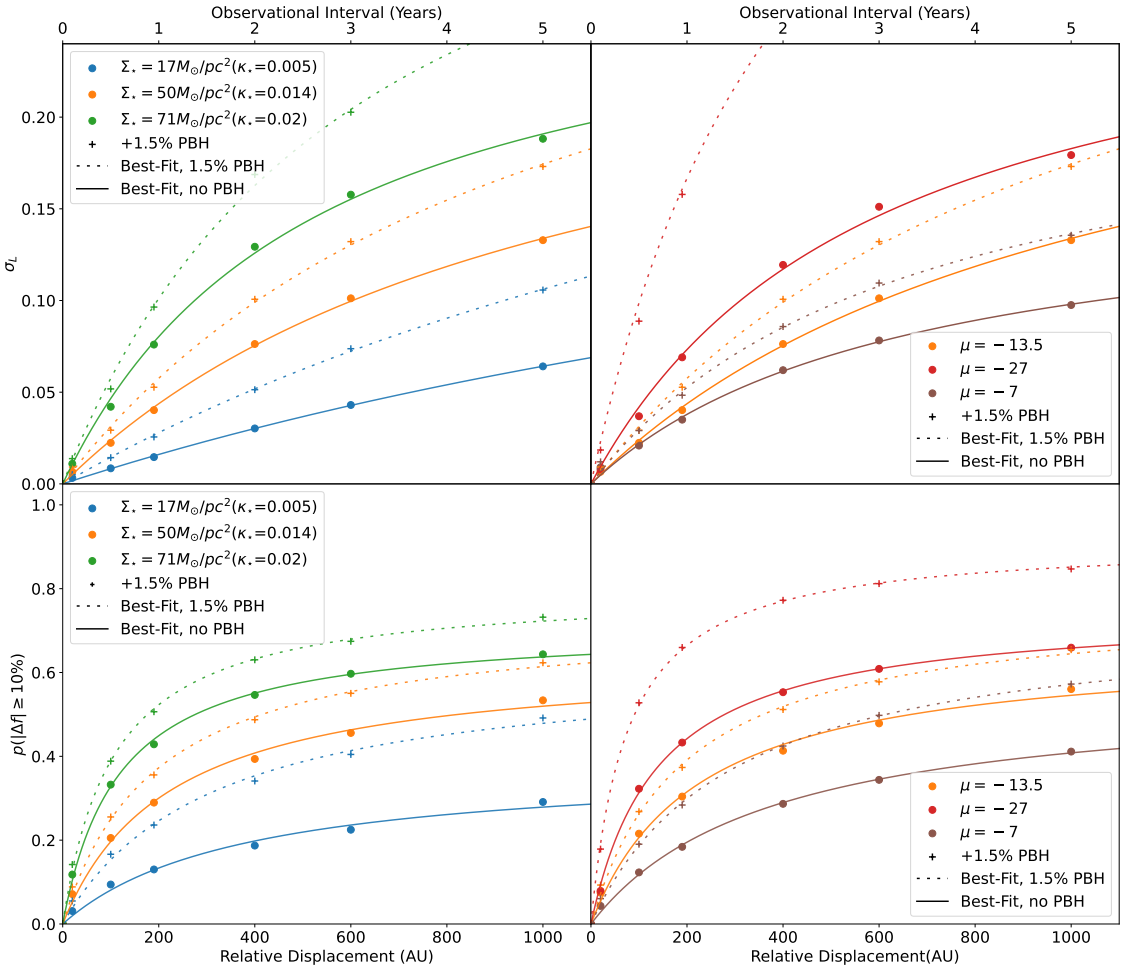

Figure 8. The best-fit Lorentzian scaling parameter σ_L (top panels) and the probability of having more than 10% change in brightness (bottom panels), both as a function of the relative displacement between two epochs. On the left, we plot simulations with fixed macro-magnification $\mu = -13.5$ and different surface mass densities; On the right, we plot simulations with fixed surface mass density of $\Sigma_\star = 50 M_\odot/\mathrm{pc}^2$ (equivalent to $\kappa_\star = 0.014$) and different macro-magnifications. For reference, the scenario of $\Sigma_\star = 50 M_\odot/\mathrm{pc}^2$ ($\kappa_\star = 0.014$) and $\mu = -13.5$ is present in both panels in orange color. Dots represent simulation done without PBHs, with configuration indicated by their color as described in the legend. Crosses represent the same setup indicated by their color in the legend but with an additional contribution to microlenses of 1.5% of DM as $30 M_\odot$ PBHs ($\kappa_{\mathrm{PBH}\approx 0.012}$). The colored lines are the best-fit Sigmoid functions of the corresponding data point, solid lines show the best fits when PBHs are not added, while short-dashed lines are the best fits when PBHs are added.

Figure 8, the dependence of $p(|\Delta f| \geq 10\%)$ with either $\Sigma_\star$ or μ can be well approximated by Sigmoid functions as expressed by the equation:

$$p(|\Delta f| \geq 10\%) \approx \frac{D}{K_p + a_p D}, \quad D > 0 \qquad (3)$$

where K_p and a_p are again the two constants of the two Sigmoid functions. The best-fit Sigmoid functions to our simulation results as indicated by the color points are indicated by the corresponding color curves.

To make Equations 2 and 3 more generally applicable, first we normalise D to a characteristic Einstein Radius of $\theta_{\mathrm{ein}} = 210\mathrm{AU}$ ($M \approx 0.0118 M_\odot$ for a lens redshift of $z = 0.375$ and a source redshift of $z = 0.7251$), such that $\delta = D/\theta_{\mathrm{ein}}$. A transverse displacement of 210 AU is that expected over a year for a relative transverse velocity of 1000 km s^{-1} between a galaxy cluster and a background

galaxy (see Section 5.1.3). Second, the best-fit Sigmoid functions are related to both the macro-magnification (μ) and the stellar surface density ($\Sigma_\star$) as they combine to create the microcaustic network. These two parameters can be reduced into one single parameter known as the effective surface mass density or the microlensing optical depth, defined as $\Sigma_{\rm eff} = \mu\Sigma_\star$ (Diego et al. 2018; Oguri et al. 2018; Dai 2021; Palencia et al. 2023). To eliminate the effect of lensing geometry, we normalized $\Sigma_{\rm eff}$ with the critical surface mass density $\Sigma_{\rm crit}$ [1]. This converts the effective surface mass density into the form of convergence, $\kappa_{\rm eff}$, and allows one to extrapolate the result to scenarios with different critical surface mass densities. With these simplifications, the constants in sigmoid function now solely depend on $\kappa_{\rm eff}$, as shown in Figure 9.

In Figure 9, we plot out all the "K"s and "a"s as functions of $\kappa_{\rm eff}$ and approximate them as power laws:

$$K = S_K \times \kappa_{\rm eff}^{\gamma_K}, \quad 0 \leq \kappa_{\rm eff} \leq 1 \tag{4}$$

$$a = S_a \times \kappa_{\rm eff}^{\gamma_a}, \quad 0 \leq \kappa_{\rm eff} \leq 1 \tag{5}$$

where S and γ are the coefficients and the exponents of the power law fit respectively, with the subscript denoting if it is the fit of the Sigmoid function constants K or a. The best-fit functions are shown in the legends of Figure 9.

By substituting the best-fit coefficients back to the Sigmoid functions and rearranging the terms, we yield two relations:

$$p(|\Delta f| \geq 10\%) \approx \frac{\kappa_{\rm eff}}{0.3\delta^{-1} + 1.1\kappa_{\rm eff}^{0.8}} \tag{6}$$

$$\sigma_L \approx \frac{\kappa_{\rm eff}^{0.9}}{3.8\delta + 1.8\kappa_{\rm eff}^{0.45}} \tag{7}$$

for which both parameters scale with $\kappa_{\rm eff}$ to the first order. These equations could be used to estimate $p(|\Delta f| \geq 10\%)$ and σ_L by substituting different values of $\kappa_{\rm eff}$ and normalized relative displacement δ under the boundary condition $\delta > 0$ and $0 \leq \kappa_{\rm eff} \leq 1$. To illustrate the behavior of the equations, we plotted out Equation 6 with different δ and $\kappa_{\rm eff}$ in Figure 10 where the full discussion regarding these equations can be found in the Appendix.

5.3. *Predicted Event rate of Stellar Microlensing*

Real observations can be compared with our model and simulations. We begin in subsection, 5.3.1 with

[1] $\Sigma_{\rm crit} = 3615 M_\odot/{\rm pc}^2$ for lens and source redshift of 0.375 and 0.7251

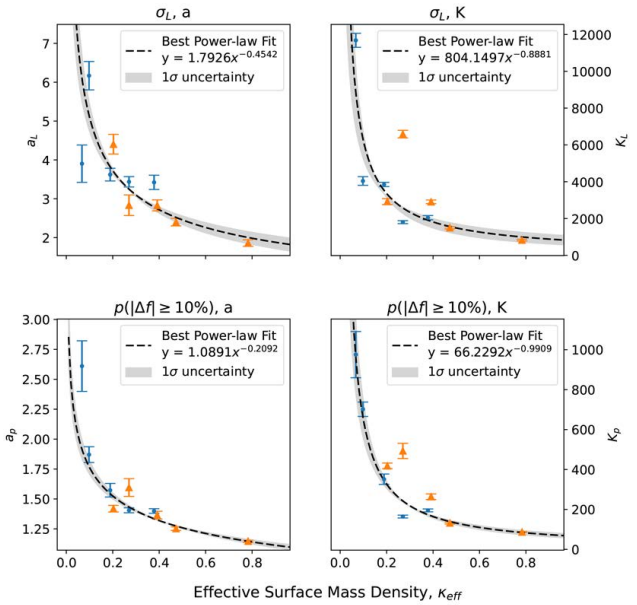

Figure 9. Best fits to the parameters of the Sigmoid functions (Equation 3 and 2) in Figure 8. The x-axis shows the effective surface mass density scaled by the critical surface density. The different plots show the first to the a parameter of σ_L (top left); K constant of σ_L (top right); a constant of probability in observing a transient (bottom left); K constant of probability in observing a transient (bottom right). The best-fit coefficients are shown in the legend, and the gray band is the 1σ uncertainty in the fitting. Blue dots are for simulations with no PBHs, and orange triangles are simulations with $f(M) = 1.5\%$

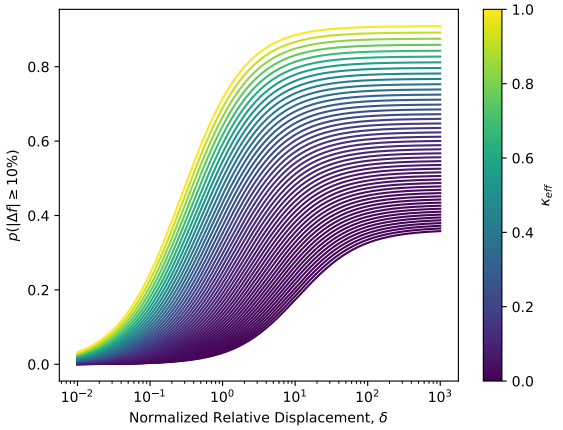

Figure 10. Equation 6, $p(|\Delta f| \geq 10\%)$ plotted as a function of δ for different values of $\kappa_{\rm eff}$ (color scale). This demonstrates the scaling with $\kappa_{\rm eff}$.

the pattern seen in the brightness variation of the three counterimages in system 2.6. If the brightness variation observed in knot 2.6.2 is caused by microlensing, then

the variation of brightness (if any) in the other counterimages of 2.6 would also be extrinsic. We then can compare if observations on system 2.6 align with one's expectation from microlensing; We continue in subsection 5.3.2 and consider whether the transient detection rate in the entire Dragon Arc aligns with the predicted rate of our simulation. Apart from the knots that show brightness variation between the two observations, there are many more knots in the Dragon Arc that do not show variability. Comparing the predicted detection rate with the observation would hence tell us if microlensing explains the transients or not.

5.3.1. *Brightness Variations in System 2.6*

We begin by examining whether the brightness variation pattern observed in system 2.6 is consistent with the expectations of microlensing qualitatively. According to our simulation, the more the effective surface mass density (and therefore, the more surface mass density of stellar microlenses if the magnification is similar), the more likely a star cluster would exhibit brightness variation. Among the three counterimages in system 2.6, knot 2.6.2 has the highest surface mass density of stellar microlenses owing to the contribution from a neighboring cluster member, and also the level of brightness variation. Thus, the observation is in qualitative agreement with expectations from stellar microlensing.

To further evaluate the qualitative argument, we can employ a quantitative approach by calculating the joint probability of reproducing our observation that knot 2.6.2 is the only transient with more than 10% brightness variation among system 2.6. Using Equation 6, we can calculate $p(|\Delta f| \geq 10\%)$ in each knot given $\delta = 0.9$ for Flashlights observations (relative velocity of 1000 km s^{-1} in 330 days). For knot 2.6.2, with $\kappa_{\rm eff} = \mu \times \kappa_\star \approx 13.5 \times 0.014 = 0.189$, the transient detection probability is 29.6%. For knots 2.6.1 and 2.6.3, with $\kappa_{\rm eff} \approx 10 \times 0.003 = 0.03$, the probability is 7.2%. Considering these probabilities, the joint probability is calculated as $29.6\% \times (1-7.2\%)^2 = 25.5\%$. This suggests that there is a 25.5% chance that microlensing can explain the observation of only knot 2.6.2 exhibiting more than 10% of brightness among the three counterimages.

Moreover, we can investigate the probability that microlensing can precisely reproduce the observed brightness variation in knot 2.6.2. Instead of utilizing Equation 6, we can refer to a simulation setup specifically tailored to knot 2.6.2 ($\kappa_\star = 0.014$ and $\mu = -13.5$). In this simulation, we find that 1550 realizations fall within $\pm 1\sigma$ of the observed flux ratio (0.86 ± 0.02). Consequently, we determine that there is a 3.1% probability that microlensing can reproduce the brightness variation seen in knot 2.6.2 within 1σ observational uncertainty. Repeating the calculation for knot 2.6.1 and knot 2.6.3, we found that our simulation has a probability of 15.0% and 6.9% in reproducing the respective observed flux ratio within 1σ.

The probability of microlensing reproducing the observed flux ratio, on its own, does not provide definitive evidence for the presence of microlensing. Furthermore, with only one event based on the two Flashlights observations, it is currently impossible to verify this probability. To further investigate the nature of the observed event, an alternative approach is to assess the transient detection rate across all the knots in the Dragon Arc, as will be discussed next.

5.3.2. *Transient Detection Rate*

To assess the likelihood of microlensing being responsible for the observed young star cluster transients, we can compare the observed transient detection rate with the theoretically predicted detection rate calculated by Equation 6.

As mentioned early in Section 1, we have discovered ten lensed knot transients in the Dragon Arc. To compare with our simulation result which accounts for brightness variations of more than 10% between the two Flashlights observations, we impose the same criteria on the lensed knots transients and yield a subsample of eight transients. To compute the detection rate, we also selected a total of 55 unresolved lensed knots in the Dragon Arc (indicated by white diamonds in Figure 1) with the following criteria:

1. Away from Critical Curves predicted by our lens model such that the macro-magnification is sufficiently low ($\mu_{\rm macro} \leq 50$), this ensures that the objects are star clusters instead of individual stars as the latter would not be detectable given the low magnification.

2. Detectable in both Flashlights epochs, preferably also detectable during the HFF epoch. This further prevents caustic crossing events featuring one single star from contaminating the sample.

3. FWHM $\leq 0.08''$ such that they are unresolved.

Suppose all the lensed knot transients are indeed caused by microlensing and hence are independent events. In that case, we can estimate the uncertainty in the detection rate as the square root of the number of detections. Therefore, given that we have eight transient detections out of 55 lensed knots, the observed transient detection rate is $14.5 \pm 5.1\%$. Now, we assume that all these 55 knots have similar ages and total

masses, and also possess similar stellar mass functions. Under such an assumption, we can extrapolate our simulation result to compare with the observed detection rate directly. According to our lens model, the mean macro-magnification of the selected knots in the Dragon Arc is ~ 20. Without any nearby cluster member galaxies, the surface mass density of stellar microlenses in the Dragon Arc is ~ 0.003 (see Section 5.1.1). Hence, substituting $\delta = 0.9$ and $\kappa_{\rm eff} = 0.06$ into Equation 6, the detection rate for transients with flux variation exceeding 10% in the Flashlights observations is estimated to be 12.9%. This is in good agreement with and well within the observational uncertainty of the detection rate.

The good agreement between the theoretical and observed transient detection rates implies that stellar microlensing alone can explain all the lensed knot transients detected, without the need for additional microlenses like primordial black holes (PBHs), or other sources of brightness variation such as stellar outbursts. Furthermore, we can calculate the probability that a transient event involving lensed young star clusters is caused by microlensing using Bayesian statistics:

$$P(\mu L|Tr) = \frac{P(Tr|\mu L)P(\mu L)}{P(Tr)}, \tag{8}$$

where μL and Tr denotes microlensing and transient detection respectively.

From the earlier discussion, the probability of detecting a transient due to microlensing, $P(Tr|\mu L)$, is 12.9%. The transient detection rate, $P(Tr)$, is 14.5 ± 5.1%. Since microlensing always acts on lensed knots, even though the flux ratio is around unity for most of the time, $P(\mu L) = 100$%. These combine to give $P(\mu L|Tr)$, the probability of an observed lensed knot transient being a microlensing event, to be 89^{+11}_{-31}%. This is consistent with the conclusion that all the lensed knot transients are likely caused by stellar microlensing.

6. DISCUSSION

6.1. *Effect from millilenses*

Substructure in the lens plane, for instance, globular clusters from the intracluster medium overlapping in position with the Dragon Arc can provide a boost to the magnification. A detailed study of the effect of millilenses is beyond the scope of this paper but we can use simple arguments to discuss their effects. Adopting a globular cluster as the model for a millilens, around this globular cluster a critical curve can form around it and where the magnification can be sufficiently large to make $\kappa_{\rm eff}$ close to unity and maximize the microlensing effects. Hence, at the position of these millilenses, we expect to see an enhanced rate of microlensing events, even if the macro model magnification from the cluster is relatively small. Hence we may expect to see microlensing events at relatively large offsets from the cluster critical curve provided there is GC at that position.

To better discuss the role of millilenses, we show in Figure 11 the caustics for a source at $z = 0.7251$ of a millilens at $z = 0.375$ with mass $M = 2 \times 10^3\,{\rm M}_\odot$ and in a region of the lens plane with macromodel magnification 23. That is, this millilens is in a portion of the lens plane where the macro model magnification is relatively small compared with the magnification near the cluster critical curves. This situation is similar to the transient knot 2.6.2. The scale of the caustic region is ≈ 1 pc for this mass. Larger millilenses or larger macromodel magnifications would make the caustic region larger but the relevant scaling for our case is relative to the smaller portion of the caustic with the largest magnification factors.

Most of the caustic region associated with the milliens has moderate magnification (within a factor 2 from the macromodel value). Only the small regions in the cusps or very close to the thin caustic lines can have large magnification factors. At $\mu > 100$ the value of $\kappa_{\rm eff}$ is sufficiently large that microlensing events can have a high probability. To estimate the probability of this happening, we compute the area with a magnification greater than a given value and find that for $\mu > 50$ this scales as $A(>\mu) \approx 0.02(100/\mu)^2$ pc^2 for this millilens. Assuming the background young star cluster spans tens of parsecs, the millilens would have a relatively small effect on the net magnification of the entire young star cluster since only a small portion of the young star cluster can have large magnification factors. However, the stars in this small region can be highly magnified and have a high probability of microlensing which would temporarily boost the magnification even more.

The discussion presented above is for a relatively small millilens. For a millilens 100 times heavier, the area above magnification $\mu = 100$ would scale linearly with the mass (Diego et al. 2018; Palencia et al. 2023; Diego 2024), that is, we would expect ≈ 2 pc^2 where microlensing events can take place with high probability.

Based on our earlier calculations in Section 5.1, we estimate the number density of luminous stars ($M \lesssim -8$) to be ~ 0.02 stars per pc^2 in a young star cluster. We then expect one in every 25 GCs with mass $2 \times 10^5\,{\rm M}_\odot$ and aligned with a young star cluster to produce a microlensing event at any given point.

6.2. *Luminous Blue Variables*

Despite stellar microlensing's success in explaining all the lensed young star cluster transients detected in the

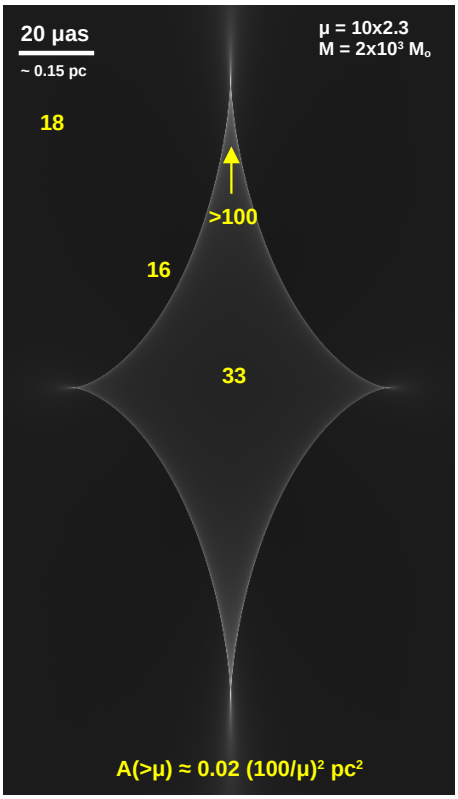

Figure 11. Millicaustic around a small millilens with mass $M = 2{\times}10^3 M_\odot$ in a region of the lens plane with macromodel magnification 23. Numbers in yellow indicate the typical magnification at that position. The area with magnification greater than 100 is very small (≈ 0.02 pc^2) and concentrated around the thin caustic lines and cusps. For macromodel magnification -13 the area would be a factor $(23/13)^2$ times smaller.

Dragon Arc ($P(\mu L|Tr) = 89^{+11}_{-31}\%$, we cannot completely rule out the possibility that some of the transients are caused by intrinsic variability. Here, we consider whether the level of variations observed (where definitive) is compatible with a stellar outburst.

Apart from novae or supernovae, the optically brightest stellar outbursts are Luminous Blue Variables (LBVs). LBVs are bright, supergiant stars that undergo stellar outbursts in irregular manners (See Humphreys & Davidson 1994; Smith et al. 2011; Kalari et al. 2018, for a detailed review) whose mechanisms are not yet fully understood. With these stellar outbursts, LBVs were found to be capable of explaining some of the transients detected in the literature (e.g., Diego et al. 2022). These young stars exist in young star clusters and therefore have the potential to explain some of the observed lensed young star cluster transients found in our work.

LBVs span a wide range of luminosity between $-8.5 \lesssim M_V \lesssim -11$ (Weis & Bomans 2020) with Black Body temperature spanning between $15,000 - 20,000K$ depending on their phase of variability (Kalari et al. 2018). For such a range of effective temperatures, the V band magnitude of an LBV at $z = 0$ is almost the same as their F200LP magnitude at $z = 0.7251$. This fact allowed us to compare the F200LP magnitude of LBVs (if any) in the Dragon Arc with the well-studied V band magnitude in the literature. Earlier, we have shown that knot 2.6.2 exhibited a change in magnitude of $\Delta m_{F200LP} = 0.16 \pm 0.02$ between the two Flashlights epochs ($\sim$ 190 days in the rest frame). If this variation originates from an LBV, it is implied that the actual change in brightness of the LBV has to be larger than $\Delta m_{F200LP} = 0.16$. For example, an LBV with $M_{F200LP} \geq -11$ contributes $\lesssim 1/4$ of the brightness of a young star cluster with $M_{F200LP} = -12.5$, the change in brightness of the young star cluster then corresponds to $\Delta m_{F200LP} \gtrsim 0.5$ of the LBV. Such variation and time scale agree with the S-Doradus variability of LBVs, which vary between $\pm \sim 1$ magnitude over a time scale from year to decade (Kalari et al. 2018).

From the above argument, we found that LBV can explain the brightness variation of system 2.6 in the Flashlights observations. With that said, we would emphasize that it would be very unlikely that LBV alone can explain all the lensed young star cluster transients we observed. Extrapolating the number density of LBV that has been active over the past decades in the nearby star-forming galaxies with multiple young star clusters (e.g., M31 and M33, Richardson & Mehner 2018), similar to the Dragon Arc galaxy, one expects only one to three active LBVs in the Dragon Arc. Since the pattern of outbursts in LBV is highly aperiodic and not well studied, we cannot estimate precisely the chance of observing an LBV outburst among all the young star clusters in the Dragon Arc. However, the fact that we observed ten transients out of 55 young star clusters (although some are counted multiple times due to their multiply-lensed nature) outnumber the expected number of possibly active LBVs from the local universe, making LBVs unlikely to explain all the transient simultaneously.

7. CONCLUSIONS

The ongoing Flashlights program with Hubble has discovered a dozen transient events in lensed galaxies behind Abell 370, by comparing the two visits in 2020 and 2021. In addition to the caustic crossing transient candidates revealed by Flashlights, we have also found transient flux variation for several multiply-lensed young star clusters in the Dragon Arc. The nature of these young star cluster transients is interesting and not well understood. In this paper, we have employed a range of different methods to determine whether microlensing

or intrinsic stellar outbursts/variability is favored for all the transients in the Dragon Arc:

1. We have constructed a simply parameterized lens model that we refine around the Dragon Arc using all the currently identified multiple images of lensed galaxies and their redshift measurements.

2. With this improved lens model, we have first focussed on system 2.6 where two of the three counterimages are classified as transients. With the time delay and lensing magnification predicted by the lens model, we construct the light curve of system 2.6 and look for evidence of intrinsic variability. Due to uncertainties in the lens model we can not confirm or reject the intrinsic variability hypothesis We have also searched for chromaticity in system 2.6 during the HFF and found no evidence. Further monitoring of this system with Hubble and JWST is needed in order to derive a definitive conclusion regarding this interesting source.

3. We rely on microlensing simulations to derive a semi-analytical approximation of the detection rate of lensed young star cluster transients. We find that the expected event detection rate of 12.9% agrees well with the observed rate $14.4 \pm 5.5\%$ to within 1σ. Furthermore, using Bayesian statistics and our simulations, we calculate the probability that the transients we observe are caused by microlensing to be $89^{+11}_{-31}\%$. We conclude that it is highly likely that lensed young star cluster transients can be caused by stellar microlensing given the depth of our photometry.

With these tests, we conclude that stellar microlensing alone is sufficient to explain the transients observed in the lensed young star clusters of the Dragon Arc, and that no intrinsic variability is needed. However, this does not rule out the possibility that some of the transients could be intrinsically variable (for instance stellar outbursts from stars such as LBVs), which are also able to reproduce the level of flux variation seen in both Flashlights and HFF epochs and are expected to contribute to the observed rate of transient events to some degree.

Guided by our simulations, we argue that the degeneracy between microlensing and intrinsic variability (regarding the number of transeints observed in lensed young star clusters) can be resolved with JWST multiband observations over a longer baseline. JWST will provide color information and deeper photometry (more fainter events), so that any transient chromaticity is much more detectable to allow distinguishing between the two hypotheses.

ACKNOWLEDGEMENT

We thank Juno Li, Arsen Levitskiy, and Josh Zhang for the many useful discussions for this work.

S.K. Li, J. Lim, T.Broadhurst and A. Chow acknowledge the Collaborative Research Fund under grant C6017-20G, which is issued by the Research Grants Council of Hong Kong S.A.R. J.M.D. acknowledges the support of project PID2022-138896NB-C51 (MCIU/AEI/MINECO/FEDER, UE) Ministerio de Ciencia, Investigación y Universidades.

This research is based on observations made with the NASA/ESA Hubble Space Telescope obtained from the Space Telescope Science Institute, which is operated by the Association of Universities for Research in Astronomy, Inc., under NASA contract NAS 5–26555. These observations are associated with program(s) GO-14038, 15117, 15936 and 16278.

We acknowledge the usage of the following programs: Astropy (Astropy Collaboration et al. 2013, 2018), Numpy (Harris et al. 2020), Matplotlib (Hunter 2007) and Scipy (Virtanen et al. 2020)

REFERENCES

Abbott, B. P., Abbott, R., Abbott, T. D., et al. 2016, Phys. Rev. Lett., 116, 061102, doi: 10.1103/PhysRevLett.116.061102

Astropy Collaboration, Robitaille, T. P., Tollerud, E. J., et al. 2013, A&A, 558, A33, doi: 10.1051/0004-6361/201322068

Astropy Collaboration, Price-Whelan, A. M., Sipőcz, B. M., et al. 2018, AJ, 156, 123, doi: 10.3847/1538-3881/aabc4f

Bacon, R., Accardo, M., Adjali, L., et al. 2010, in Society of Photo-Optical Instrumentation Engineers (SPIE) Conference Series, Vol. 7735, Ground-based and Airborne Instrumentation for Astronomy III, ed. I. S. McLean, S. K. Ramsay, & H. Takami, 773508, doi: 10.1117/12.856027

Bird, S., Cholis, I., Muñoz, J. B., et al. 2016, Phys. Rev. Lett., 116, 201301, doi: 10.1103/PhysRevLett.116.201301

Carnall, A. C., McLure, R. J., Dunlop, J. S., & Davé , R. 2018, Monthly Notices of the Royal Astronomical Society, 480, 4379, doi: 10.1093/mnras/sty2169

Chabrier, G. 2003, PASP, 115, 763, doi: 10.1086/376392

Chen, W., Kelly, P. L., Diego, J. M., et al. 2019, The Astrophysical Journal, 881, 8, doi: 10.3847/1538-4357/ab297d

Chow, A., Li, S. K., Lim, J., et al. 2024, ApJ, 962, 30, doi: 10.3847/1538-4357/ad1246

Dai, L. 2021, Monthly Notices of the Royal Astronomical Society, 501, 5538, doi: 10.1093/mnras/stab017

de Oliveira, N. O. L., Jiménez-Teja, Y., & Dupke, R. 2022, Monthly Notices of the Royal Astronomical Society, 512, 1916, doi: 10.1093/mnras/stac407

Diego, J. M. 2024

Diego, J. M., Pascale, M., Kavanagh, B. J., et al. 2022, Astronomy & Astrophysics. https://api.semanticscholar.org/CorpusID:247476158

Diego, J. M., Kaiser, N., Broadhurst, T., et al. 2018, The Astrophysical Journal, 857, 25, doi: 10.3847/1538-4357/aab617

Diego, J. M., Schmidt, K. B., Broadhurst, T., et al. 2018, MNRAS, 473, 4279, doi: 10.1093/mnras/stx2609

Diego, J. M., Sun, B., Yan, H., et al. 2023, A&A, 679, A31, doi: 10.1051/0004-6361/202347556

Diego, J. M., Li, S. K., Meena, A. K., et al. 2023, BUFFALO/Flashlights: Constraints on the abundance of lensed supergiant stars in the Spock galaxy at redshift 1. https://arxiv.org/abs/2304.09222

Duric, N. 2004, Advanced astrophysics, Vol. 1 (Cambridge University Press)

Filippis, E. D., Sereno, M., & Bautz, M. 2005, Advances in Space Research, 36, 715, doi: 10.1016/j.asr.2004.12.078

Ghosh, A., Williams, L. L. R., Liesenborgs, J., et al. 2021, MNRAS, 506, 6144, doi: 10.1093/mnras/stab1196

Harris, C. R., Millman, K. J., van der Walt, S. J., et al. 2020, Nature, 585, 357, doi: 10.1038/s41586-020-2649-2

Humphreys, R. M., & Davidson, K. 1994, PASP, 106, 1025, doi: 10.1086/133478

Hunter, J. D. 2007, Computing in Science & Engineering, 9, 90, doi: 10.1109/MCSE.2007.55

Kalari, V. M., Vink, J. S., Dufton, P. L., & Fraser, M. 2018, Astronomy & Astrophysics, 618, A17, doi: 10.1051/0004-6361/201833484

Keeton, C. R. 2001, A Catalog of Mass Models for Gravitational Lensing, arXiv, doi: 10.48550/ARXIV.ASTRO-PH/0102341

Keeton, C. R., Kochanek, C. S., & Seljak, U. 1997, The Astrophysical Journal, 482, 604, doi: 10.1086/304172

Kelly, P. L., Diego, J. M., Rodney, S., et al. 2018, Nature Astronomy, 2, 334, doi: 10.1038/s41550-018-0430-3

Kelly, P. L., Chen, W., Alfred, A., et al. 2022, Flashlights: More than A Dozen High-Significance Microlensing Events of Extremely Magnified Stars in Galaxies at Redshifts z=0.7-1.5, arXiv, doi: 10.48550/ARXIV.2211.02670

Kelly, P. L., Rodney, S., Treu, T., et al. 2023, Science, 380, doi: 10.1126/science.abh1322

Kroupa, P. 2001, MNRAS, 322, 231, doi: 10.1046/j.1365-8711.2001.04022.x

Lagattuta, D. J., Richard, J., Clément, B., et al. 2017, Monthly Notices of the Royal Astronomical Society, 469, 3946–3964, doi: 10.1093/mnras/stx1079

Lagattuta, D. J., Richard, J., Bauer, F. E., et al. 2019, Monthly Notices of the Royal Astronomical Society, doi: 10.1093/mnras/stz620

Lotz, J. M., Koekemoer, A., Coe, D., et al. 2017, The Astrophysical Journal, 837, 97, doi: 10.3847/1538-4357/837/1/97

Meena, A. K., Zitrin, A., Jimé nez-Teja, Y., et al. 2023a, The Astrophysical Journal Letters, 944, L6, doi: 10.3847/2041-8213/acb645

Meena, A. K., Chen, W., Zitrin, A., et al. 2023b, Monthly Notices of the Royal Astronomical Society, 521, 5224, doi: 10.1093/mnras/stad869

Miralda-Escude, J. 1991, ApJ, 379, 94, doi: 10.1086/170486

Molnar, S. M., Ueda, S., & Umetsu, K. 2020, The Astrophysical Journal, 900, 151, doi: 10.3847/1538-4357/abac53

Morishita, T., Abramson, L. E., Treu, T., et al. 2017, ApJ, 846, 139, doi: 10.3847/1538-4357/aa8403

Navarro, J. F., Frenk, C. S., & White, S. D. M. 1997, The Astrophysical Journal, 490, 493, doi: 10.1086/304888

Negueruela, I., Alfaro, E. J., Dorda, R., et al. 2022, A&A, 664, A146, doi: 10.1051/0004-6361/202142985

Oemler, Augustus, J., Dressler, A., & Butcher, H. R. 1997, ApJ, 474, 561, doi: 10.1086/303472

Oguri, M. 2010, PASJ, 62, 1017, doi: 10.1093/pasj/62.4.1017

Oguri, M. 2021, Publications of the Astronomical Society of the Pacific, 133, 074504, doi: 10.1088/1538-3873/ac12db

Oguri, M., Diego, J. M., Kaiser, N., Kelly, P. L., & Broadhurst, T. 2018, Physical Review D, 97, doi: 10.1103/physrevd.97.023518

Oke, J. B., & Gunn, J. E. 1983, ApJ, 266, 713, doi: 10.1086/160817

Palencia, J. M., Diego, J. M., Kavanagh, B. J., & Martinez, J. 2023, Statistics of magnification for extremely lensed high redshift stars. https://arxiv.org/abs/2307.09505

Richard, J., Kneib, J.-P., Limousin, M., Edge, A., & Jullo, E. 2010, Monthly Notices of the Royal Astronomical Society: Letters, 402, L44, doi: 10.1111/j.1745-3933.2009.00796.x

Richard, J., Claeyssens, A., Lagattuta, D., et al. 2021, Astronomy & Astrophysics, 646, A83, doi: 10.1051/0004-6361/202039462

Richardson, N. D., & Mehner, A. 2018, Research Notes of the AAS, 2, 121, doi: 10.3847/2515-5172/aad1f3

Rodney, S. A., Balestra, I., Bradac, M., et al. 2018, Nature Astronomy, 2, 324, doi: 10.1038/s41550-018-0405-4

Salpeter, E. E. 1955, ApJ, 121, 161, doi: 10.1086/145971

Schauer, A. T. P., Bromm, V., Drory, N., & Boylan-Kolchin, M. 2022, On the probability of the extremely lensed z=6.2 Earendel source being a Population III star, arXiv, doi: 10.48550/ARXIV.2207.02863

Sérsic, J. L. 1963, Boletin de la Asociacion Argentina de Astronomia La Plata Argentina, 6, 41

Smith, N., Li, W., Silverman, J. M., Ganeshalingam, M., & Filippenko, A. V. 2011, Monthly Notices of the Royal Astronomical Society, 415, 773, doi: 10.1111/j.1365-2966.2011.18763.x

Soto, K. T., Lilly, S. J., Bacon, R., Richard, J., & Conseil, S. 2016, Monthly Notices of the Royal Astronomical Society, 458, 3210, doi: 10.1093/mnras/stw474

Soucail, G., Fort, B., Mellier, Y., & Picat, J. P. 1987a, A&A, 172, L14

Soucail, G., Mellier, Y., Fort, B., Hammer, F., & Mathez, G. 1987b, A&A, 184, L7

Soucail, G., Mellier, Y., Fort, B., Mathez, G., & Cailloux, M. 1987c, The Messenger, 50, 5

—. 1988, A&A, 191, L19

Strait, V., Bradač, M., Hoag, A., et al. 2018, ApJ, 868, 129, doi: 10.3847/1538-4357/aae834

Struble, M. F., & Rood, H. J. 1999, The Astrophysical Journal Supplement Series, 125, 35, doi: 10.1086/313274

Treu, T., Schmidt, K. B., Brammer, G. B., et al. 2015, ApJ, 812, 114, doi: 10.1088/0004-637X/812/2/114

Venumadhav, T., Dai, L., & Miralda-Escudé , J. 2017, The Astrophysical Journal, 850, 49, doi: 10.3847/1538-4357/aa9575

Virtanen, P., Gommers, R., Oliphant, T. E., et al. 2020, Nature Methods, 17, 261, doi: 10.1038/s41592-019-0686-2

Weis, K., & Bomans, D. J. 2020, Galaxies, 8, doi: 10.3390/galaxies8010020

Williams, L. L. R., Kelly, P. L., Treu, T., et al. 2023, Flashlights: Properties of Highly Magnified Images Near Cluster Critical Curves in the Presence of Dark Matter Subhalos. https://arxiv.org/abs/2304.06064

APPENDIX

A. MULTIPLY LENSED IMAGE SYSTEMS

The positions and redshifts of the multiply-lensed image systems as described in Section 3. The redshifts are spectroscopic unless denoted with asterisks (photometric/model-fitted).

Table 5. List of Multiply-Lensed Images in A370

ID	Ra	Dec	Redshift
1.1	39.976273	-1.5760558	0.8041
1.2	39.968691	-1.5766113	0.8041
1.3	39.967047	-1.5769172	0.8041
2.1.1	39.973825	-1.584229	0.7251
2.1.2	39.971003	-1.5850422	0.7251
2.1.3	39.96963	-1.5848508	0.7251
2.1.4	39.969394	-1.5847328	0.7251
2.1.5	39.968722	-1.5845058	0.7251
2.2 - 2.10 (1)	–	–	0.7251
3.1	39.978925	-1.5674624	1.9553
3.2	39.968526	-1.5657906	1.9553
3.3	39.965658	-1.566856	1.9553
4.1	39.979704	-1.5764364	1.2728
4.2	39.970688	-1.5763221	1.2728
4.3	39.961971	-1.5779671	1.2728
5.1	39.973473	-1.5890463	1.2775
5.2	39.970576	-1.5891946	1.2775
5.3	39.969472	-1.5890961	1.2775
5.4	39.96858	-1.5890045	1.2775
6.1	39.979641	-1.5770904	1.0633
6.2	39.969405	-1.5771811	1.0633
6.3	39.964334	-1.5782307	1.0633
7.1	39.986567	-1.5775688	2.7512
7.2	39.969882	-1.5807608	2.7512
7.3	39.969788	-1.5804299	2.7512
7.4	39.969046	-1.5774833	2.7512
7.5	39.968815	-1.5856313	2.7512
7.6	39.968454	-1.5715778	2.7512
7.7	39.968142	-1.5710778	2.7512
7.8	39.961533	-1.5800028	2.7512
8.1	39.964485	-1.5698065	2.884*
8.2	39.961889	-1.5736473	2.884*
9.1	39.982022	-1.5765337	1.5182
9.2	39.969486	-1.5762654	1.5182
9.3	39.962402	-1.5778911	1.5182
10.1	39.98846	-1.5719676	7.04*
10.2	39.963839	-1.5693802	7.04*
10.3	39.960789	-1.5741702	7.04*
11.1	39.9841	-1.5709127	3.4809
11.2	39.969682	-1.566636	3.4809
11.3	39.959198	-1.5753221	3.4809
12.1	39.979513	-1.5717782	4.248
12.2	39.97521	-1.5688203	4.248
12.3	39.956759	-1.5775032	4.248
13.1	39.981313	-1.5782202	3.1309
13.2	39.974254	-1.585577	3.1309
13.3	39.972309	-1.578091	3.1309
13.4	39.972192	-1.5801027	3.1309
13.5	39.957673	-1.580459	3.1309
14.1	39.984008	-1.5784556	3.7084
14.2	39.971935	-1.5870512	3.7084
14.3	39.971328	-1.580604	3.7084
14.4	39.971027	-1.5777907	3.7084
14.5	39.970450	-1.5689437	3.7084
14.6	39.970391	-1.5696387	3.7084
14.7	39.958795	-1.5805488	3.7084
15.1	39.984414	-1.5841111	3.7743
15.2	39.964016	-1.5880782	3.7743
16.1	39.985403	-1.5808406	4.2567
16.2	39.969758	-1.5885333	4.2567
16.3	39.960235	-1.5836508	4.2567
17.1	39.981476	-1.5820728	4.4296
17.2	39.97583	-1.5870613	4.4296
17.3	39.957362	-1.5820861	4.4296
18.1	39.985142	-1.5790944	5.6493
18.2	39.971996	-1.5878654	5.6493
18.3	39.958316	-1.5813093	5.6493
19.1	39.965279	-1.5878055	5.7505
19.2	39.963619	-1.5868798	5.7505
20.1	39.981539	-1.5814028	1.2567
20.2	39.967252	-1.5849694	1.2567
20.3	39.966733	-1.5846943	1.2567
21.1	39.981675	-1.5796852	3.1309
21.2	39.974406	-1.5861017	3.1309
21.3	39.957906	-1.5810108	3.1309
22.1	39.980113	-1.5667264	5.9386
22.2	39.977166	-1.5662748	5.9386
22.3	39.957315	-1.572744	5.9386
23.1	39.963111	-1.570603	4.916
23.2	39.96204	-1.5723407	4.916
24.1	39.987084	-1.5790992	3.8145
24.2	39.966982	-1.5867999	3.8145
24.3	39.961703	-1.5832126	3.8145
25.1	39.979924	-1.571393	3.9359
25.2	39.97446	-1.5680963	3.9359
25.3	39.95717	-1.5769717	3.9359
26.1	39.980691	-1.5711198	3.0161
26.2	39.97244	-1.5671511	3.0161
26.3	39.958292	-1.5759068	3.0161
27.1	39.987817	-1.5774528	2.9101
27.2	39.967058	-1.5845583	2.9101
27.3	39.963492	-1.5822806	2.9101

Table 5 *continued*

Table 5 *(continued)*

Table 5 *continued*

Table 5 *(continued)*

ID	Ra	Dec	Redshift
28.1	39.983596	-1.5674774	4.4897
28.2	39.968425	-1.5646657	4.4897
28.3	39.960838	-1.5691328	4.4897
29.1	39.983351	-1.5704081	5.6459
29.2	39.972404	-1.5663533	5.6459
30.1	39.980667	-1.5747346	5.4476
30.2	39.97475	-1.5693301	5.4476
30.3	39.956156	-1.5786786	5.4476
31.1	39.988097	-1.5751871	4.4953
31.2	39.966285	-1.5693446	4.4953
31.3	39.960682	-1.5783795	4.4953
32.1	39.966215	-1.5879961	4.882
32.2	39.962722	-1.5860036	4.882
33.1	39.985048	-1.579559	5.2437
33.2	39.971805	-1.5880395	5.2437
33.3	39.970107	-1.5701499	5.2437
33.4	39.958566	-1.5817008	5.2437
34.1	39.981538	-1.5658624	6.1735
34.2	39.975825	-1.5644423	6.1735
35.1	39.962444	-1.5807098	6.2855
35.2	39.965996	-1.5843845	6.2855
36.1	39.970391	-1.5687943	5.6489
36.2	39.970428	-1.5694203	5.6489
37.1	39.977154	-1.5737917	3.2
37.2	39.975063	-1.5721045	3.2
38.1	39.983162	-1.5796664	4.3381
38.2	39.973383	-1.5874465	4.3381
38.3	39.970632	-1.5710393	4.3381
38.4	39.957967	-1.5815081	4.3381
39.1	39.982296	-1.576975	1.272*
39.2	39.967933	-1.5773472	1.272*
39.3	39.965442	-1.5780222	1.272*
40.1	39.963579	-1.5656333	1.0315
40.2	39.963375	-1.5659528	1.0315
40.3	39.962958	-1.5661111	1.0315
41.1	39.984054	-1.5733556	1.973*
41.2	39.966563	-1.5696694	1.973*
41.3	39.962117	-1.57525	1.973*
42.1	39.977717	-1.5827917	2.336*
42.2	39.976646	-1.5836028	2.336*
43.1	39.982400	-1.5811	8.593*
43.2	39.975875	-1.58726	8.593*

[1] Refer to Table 3 for the positions of Systems 2.2 - 2.10

B. SPECTRA OF KNOT COUNTERPARTS IN DRAGON ARC

C. SUPPLEMENTARY MATERIALS OF MICROLENSING SIMULATION

We include the supplementary materials and discussion related to our microlensing simulation here in this section. We first evaluate the surface mass density of knot 2.6.2 contributed by a neighbor cluster member. We then introduce test carried out for validating assumptions in our simulation. At the end of this appendix section, we also discuss a few identified caveats and limitations in our simulation.

C.1. *Neighbour Cluster Member Surface Mass Density*

To determine the surface mass density associated with cluster member 5, the cluster member nearest to knot 2.6.2 (see Figure 2 for reference), we apply SED fitting with `Bagpipes` (Carnall et al. 2018) on cluster member 5 to obtain its stellar mass, and image fitting to obtain its surface brightness profile.

The best-fit SED of cluster member 5 assuming an exponential decay star formation history has a current stellar mass of $M_{stars} = 3.47 \times 10^9 M_\odot$. We then fit a 2D Sersic profile (Sérsic 1963) to cluster member 5 on the $F160W$ image which has the highest sensitivity to the light of lower-mass stars that dominate the stellar population in a cluster member galaxy. Assuming a linear relationship between brightness and stellar mass, the 2D light profile from the Sersic fit is converted to a 2D mass profile. By so doing, the surface mass density at knot 2.6.2 as contributed by cluster member 5 is estimated as $\sim 40\ M_\odot/pc^2$ ($\equiv 0.011\kappa_\star$).

C.2. *Representativeness of Simulation FOV*

As mentioned in Section 5.1, our simulation FOV (0.8 pc$\times$0.8 pc) is much smaller than the physical size of young star clusters (radius of $\sim$ 100pc). As a test to see if a smaller FOV is sufficient to represent a larger FOV and therefore the physical size of young star clusters, we repeat one of the simulations ($\kappa_\star = 0.014$, $\mu = -13.5$ and $f(M) = 0$) with a larger FOV of 1.6 pc $\times$ 1.6 pc (four times the original FOV) as shown in Figure 13. The two simulations (the orange curve for the original FOV and the blue curve for that of a larger FOV) only show an average percentage difference of 0.7%. There is no significant difference in the simulation result and we conclude that our small microcaustic map can represent a larger FOV.

C.3. *Discussion on the Semi-analytical Approximation*

Here we assess the validity of Equation 6 and Equation 7 by examining their behaviors under certain boundary conditions. For instance, if there is no net relative velocity (i.e., no time elapsed), we expect no brightness variation. This condition is satisfied when the numerator of the sigmoid functions, δ, is equal to zero. Additionally, if there are no microlenses or macro-magnification ($\kappa_{\rm eff} \to 0$), the denominator of the equations tends towards infinity, resulting in both $p(|\Delta f| \geq 10\%)$ and σ_L approaching zero. These con-

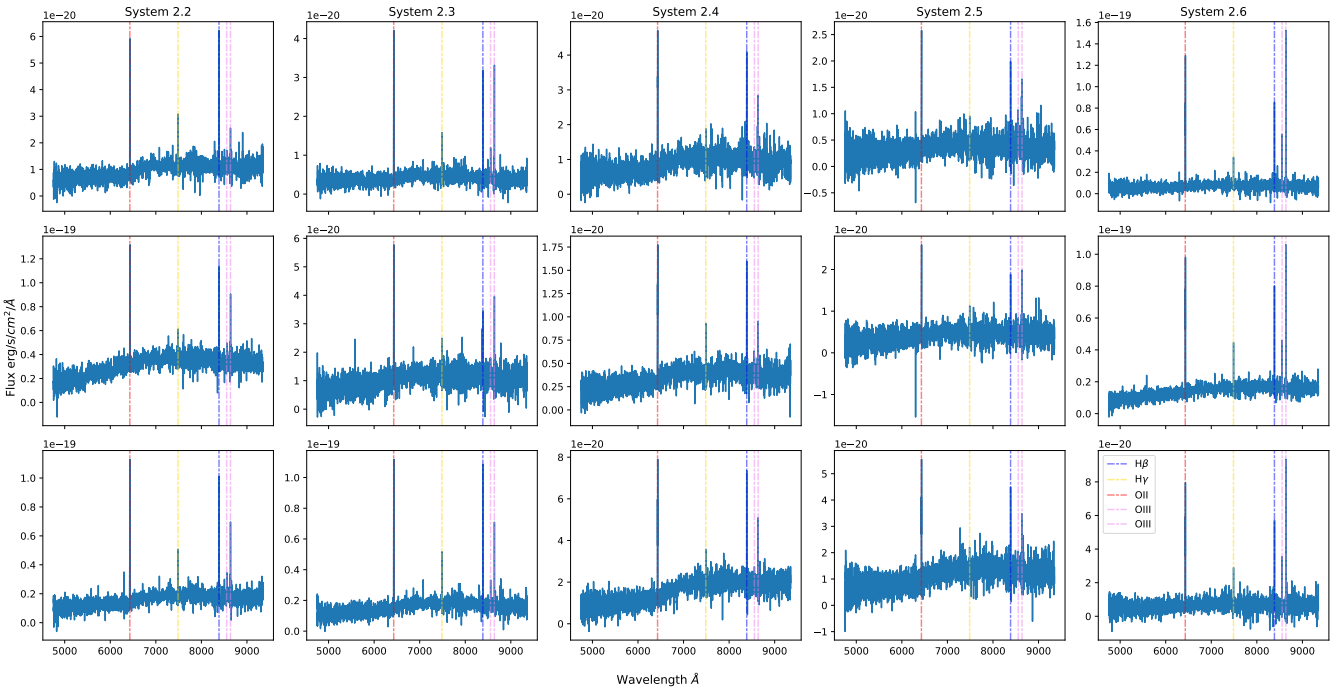

Figure 12. MUSE spectra of all the bright knots in System 2. Important lines, including Hβ, Hγ, [OII] and [OIII] doublets are indicated.

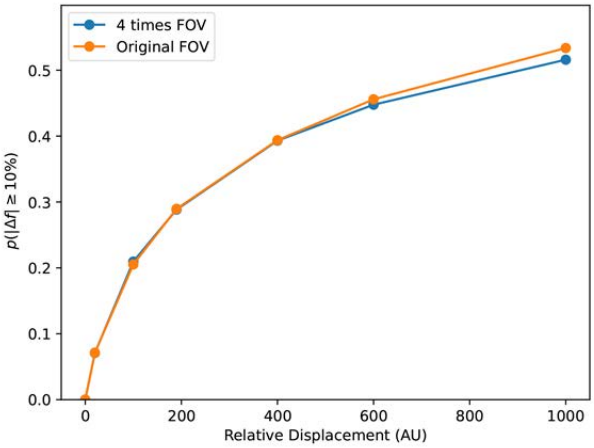

Figure 13. $p(|\Delta f| \geq 10\%)$ against the relative displacement as a test of the effect from simulation FOV. Both simulations have the same setting of $\kappa_\star = 0.014$, $\mu = -13.5$ without PBHs. The only difference between the two sets of simulation is their FOV: the orange curve is generated from a simulation FOV of 0.8 pc$\times$0.8 pc; the blue curve is generated from a simulation FOV of 1.6 pc $\times$ 1.6 pc. Both simulations show an extremely similar result with an average percentage difference of 0.7%.

ditions align with the physical expectations, confirming the physical validity of the equations.

C.3.1. *Effect of Effective Surface Mass Density*

Our simulation reveals that both $p(|\Delta f| \geq 10\%)$ and σ_L increase with effective surface mass density, $\kappa_{\rm eff}$. This is expected because an increase in $\kappa_{\rm eff}$ leads to more microcaustics and, consequently, more magnification and demagnification regions across the FOV. This leads to an increased likelihood of individual stars experiencing higher magnification ratios with the same relative displacement and thus also greater variation in the brightness of the entire stellar population.

However, both parameters cannot be infinitely large when $\kappa_{\rm eff}$ increases. As $\kappa_{\rm eff}$ increases, more microcaustics are expected to overlap, reducing the likelihood of stars experiencing a significant change in magnification. Consequently, there exists a turnover density where both the probability and σ_L reach a maximum and may even decrease thereafter. Previous studies (Oguri et al. 2018; Diego et al. 2018; Palencia et al. 2023) have identified this density as the critical surface density $\Sigma_{\rm crit}$ ($\kappa_{\rm eff} = 1$), corresponding to the point where microcaustics begin overlapping. At densities greater than the critical density, stars sweeping through experience fewer changes in magnification, resulting in decreased levels of brightness variation. As demonstrated in Figure 10, given a fixed δ, $p(|\Delta f| \geq 10\%)$ exhibits a rapid increase for small $\kappa_{\rm eff}$ values but gradually levels off as $\kappa_{\rm eff}$ approaches unity. This phenomenon was observed in earlier work, where $\kappa_{\rm eff} \approx 1$ corresponds to the saturation regime described in Diego et al. (2018) and where an increase in either the macromodel magnification or Σ_* has little impact on the statistics of magnification.

C.3.2. *Effect of Relative Displacement*

Similarly as the case of $\kappa_{\rm eff}$, both σ_L and probability also increase with δ. In a microcaustic region (e.g., Figure 6) with a low $\kappa_{\rm eff}$, the region of high magnification is much smaller compared to the region of low magnification. With a larger δ, the probability of a star experiencing a significant change in magnification between two epochs increases.

Again, the increase in $p(|\Delta f| \geq 10\%)$ and σ_L due to δ is not expected to continue indefinitely and should reach a limit at a certain value. Figure 10 demonstrates that $p(|\Delta f| \geq 10\%)$ increases exponentially for small δ values, but then sharply levels off after a specific δ. This effect depends on $\kappa_{\rm eff}$: for smaller $\kappa_{\rm eff}$, the increase in $p(|\Delta f| \geq 10\%)$ is slower and reaches saturation at a lower value; for larger $\kappa_{\rm eff}$, the increase in $p(|\Delta f| \geq 10\%)$ starts earlier and is faster, reaching saturation at a higher value. This behavior can be explained by the density of the microcaustics. A higher $\kappa_{\rm eff}$ indicates more closely packed caustics, reducing the distance between regions with high and low magnification. This explains why the saturation effect occurs earlier when $\kappa_{\rm eff}$ is higher, even though the maximum probability at the saturation point is also higher.

C.4. *Limitations*

In this section, we discuss a few recognized limitations of the simulation and if possible, also carry out tests to see if these limitations will significantly affect the result of our simulation.

C.4.1. *Lensing Parity*

One of the most important limitations to consider is that we only studied the scenario for negative parity, where $\mu_t < 0$ (usually on the inner side of the Critical Curve). In negative parity, the effect of substructure or microlensing is more pronounced compared with the positive parity ($\mu_t > 0$) as explored by literature (e.g., Oguri et al. 2018; Williams et al. 2023; Palencia et al. 2023). Based on these studies, one would expect that the microlensing flux variability in lensed young star clusters would be suppressed on the positive parity side. The exact effect, however, is left for future work to investigate further.

C.4.2. *Stellar Evolution and the Abundance of Hyperluminous Stars*

Another important limitation, as mentioned early on, is that our simulation is based on a very young stellar population (Age of $\sim$ 4 Myr) where we neglected the post-main sequence evolution. While this assumption is reasonable for a very young stellar population such as the young star clusters on the Dragon Arc, it would be interesting to test how sensitive the simulation results are towards the abundance of hyperluminous stars which depends on the slope of IMF as well as stellar evolution.

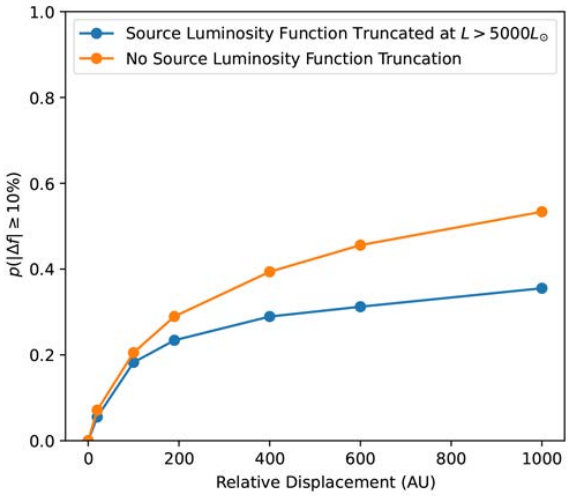

Figure 14. The detection probability of lensed transients as a function of relative displacement, where both cases feature $\mu = -13.5$ and $\kappa_\star = 0.014$. In the blue line, the source luminosity function is truncated at $L > 5000L_\odot$. In contrast, no truncation is carried out for the orange line.

To carry out the test, we examined a simple scenario where we truncated the mass of the background stellar population at $20M_\odot$ that no hyperluminous stars are allowed to exist in the stellar libraries. The test is carried with a condition where $\mu = -13.5$ and $\kappa_\star = 0.014$, with the result attached as Figure 14. As a comparison, the scenario without truncation of the luminosity function (orange curve) is also attached. The truncation leads to a decrease in the detection probability as expected. Interestingly, such a decrease is more significant at a higher relative displacement. In other words, the simulation's sensitivity towards the abundance of hyperluminous stars is lower in a small relative displacement.

The real situation could be even more complicated as it depends on the age and evolutionary model of the stellar population. A simple truncation in mass would not be a robust evaluation of the exact luminosity function in these stellar populations. These luminous stars can exist in large numbers depending on the evolutionary status of the young star cluster and allow for higher flux variability owing to microlensing. To extrapolate the results of this paper to more general scenarios, it is necessary to repeat the simulation by taking into account stellar evolution and formation history in specific stellar populations. Addressing these limitations and considering a broader range of scenarios and populations in future work will lead to a more accurate understanding of the effects of microlensing on stellar populations.